

Optical and mid-infrared neon abundance determinations in star-forming regions

Oli L. Dors Jr.^{1*}, Guillermo F. Hägele^{2,3}, Mónica V. Cardaci^{2,3},
Enrique Pérez-Montero⁴, Ângela C. Krabbe¹, José M. Vílchez⁴, Dinalva A. Sales⁵,
Rogério Riffel⁵, Rogemar A. Riffel⁶

¹ *Universidade do Vale do Paraíba, Av. Shishima Hifumi, 2911, Cep 12244-000, São José dos Campos, SP, Brazil*

² *Consejo Nacional de Investigaciones Científicas y Técnicas (CONICET), Argentina.*

³ *Facultad de Ciencias Astronómicas y Geofísicas, Universidad Nacional de La Plata, Paseo del Bosque s/n, 1900 La Plata, Argentina.*

⁴ *Instituto de Astrofísica de Andalucía (CSIC), PO Box 3004, 18080 Granada, Spain.*

⁵ *Universidade Federal do Rio Grande do Sul, IF, CP 15051, Porto Alegre 91501-970, RS, Brazil.*

⁶ *Universidade Federal de Santa Maria, Av. Roraima 1000, Cep 97105-900, Santa Maria, Brazil*

Accepted- 2011 April 28. Received -2011 February 18.

ABSTRACT

We employed observational spectroscopic data of star-forming regions compiled from the literature and photoionization models to analyse the neon ionic abundances obtained using both optical and mid-infrared emission-lines. Comparing $\text{Ne}^{++}/\text{H}^+$ ionic abundances from distinct methods, we found that, in average, the abundances obtained via IR emission-lines are higher than those obtained via optical lines by a factor of 4. Photoionization models with abundance variations along the radius of the hypothetical nebula provide a possible explanation for a large part of the difference between ionic abundances via optical and infrared emission-lines. Ionization Correction Factor (ICF) for the neon is obtained from direct determinations of ionic fractions using infrared emission-lines. A constant Ne/O ratio ($\log \text{Ne}/\text{O} \approx -0.70$) for a large range of metallicity, independently of the ICF used to compute the neon total abundance is derived.

Key words: galaxies: general – galaxies: evolution – galaxies: abundances – galaxies: formation – galaxies: ISM

1 INTRODUCTION

Gas phase metallicity determinations in star-forming regions (SFRs) have been used for the knowledge of the cosmic evolution of galaxies as well as to provide observational constraints on model parameters of galaxy formation.

In particular, the oxygen is the element most widely used for this purpose, because prominent emission lines from their main ionic stages are present in the optical spectra of SFRs (e.g. Hägele et al. 2008; Kennicutt et al. 2003, Krabbe & Copetti 2006). For the rest of elements with bright emission-lines (e.g. N, S, Ne, Ar) not all their ionic stages are observed in the optical spectrum, so their total abundances can only be calculated by means of Ionization Correction Factors (ICFs), proposed by Peimbert & Costero (1969).

Among the α -elements, Ne results of great importance

as it is one of the noble gases and it does not combine with itself or with other chemical species in the formation of molecules and, thus, dust grains. This makes the abundance determination of this element quite suitable for the study of the chemical evolution of SFRs as it does not depend on depletion factors onto dust grains. It is accepted that Ne and O are mainly produced in stars more massive than $10 M_{\odot}$ (see Woosley & Weaver 1995). Therefore, it is expected that abundances of Ne and O should closely trace one to the other (Crockett et al. 2006), and a constant Ne/O abundance ratio over a wide range of O/H abundance must be found. However, recent deep spectroscopy of a large sample of low-metallicity emission-line galaxies by Guseva et al. (2011) revealed a slight increase of Ne/O with O/H. Similar results were also found by Wang & Liu (2008) using O and Ne abundances of a sample of planetary nebulae and H II regions. In opposite, Pérez-Montero et al. (2007) derived a new ICF for Ne using a photoionization model grid finding

* E-mail:olidors@univap.br

for the high metallicity regime a slight decrease in Ne/O with O/H for a large sample of SFRs.

In any case, the derivation of the total Ne abundance has showed to be uncertain due to the difficulties estimating its ICF. The estimation of the total Ne abundance in the optical is performed via the observation of the $[\text{Ne III}]\lambda 3869$ Å emission-line, which is mainly present in SFRs with a high-ionization degree, and usually assuming an $\text{ICF}(\text{Ne}^{++})$ that is a function of the O/O^{++} ratio derived also from optical emission-lines. However, the optical $[\text{Ne III}]$ line is rarely observed in metal-rich objects (see Bresolin et al. 2005), where most of the Ne is in the form of Ne^+ , so the ionization corrections are not well constrained in this regime (Kennicutt et al. 2003). This problem can be alleviated by the use of infrared fine-structure lines (Vermeij & van der Hulst 2002). On this context, both the *Infrared Space Observatory (ISO)*, Kessler et al. 1996) and the *Spitzer Space Telescope* have allowed the observation of bright mid-infrared emission-lines in SFRs, such as $[\text{Ne II}]\lambda 12.81\mu\text{m}$ and $[\text{Ne III}]\lambda 15.56\mu\text{m}$, and the determination of the total Ne abundance simply summing the corresponding ionic fractions. For instance, Vermeij & van der Hulst (2002) used optical and mid-IR data of H II regions located in the Magellanic Clouds (see also Vermeij et al. 2002) to determine O, S, and Ne abundances in these objects. These authors found large discrepancies between Ne^{++} abundances obtained via infrared lines with those via optical temperature determinations and pointed out that the classical approximation, $\text{ICF}(\text{Ne}^{++})=\text{O}/\text{O}^{++}$ (Peimbert & Costero 1969), seems to underestimate the true Ne abundance (see also Pérez-Montero et al. 2007). However, due to large scatter and uncertainty in the Ne^{++} ionic fraction of their data, no conclusion could be drawn about the reliability of the optical ICF for Ne. The same results were obtained by Kennicutt et al. (2003), who combined the ionic abundances derived by Vermeij & van der Hulst (2002) and by Willner & Nelson-Patel (2002) for H II regions located in M 33. However, they were not able to derive a functional form for the $\text{ICF}(\text{Ne}^{++})$, due to the large scatter of the available data and the very few measurements for low-ionization regions. Fortunately, a large number of mid-IR and optical data of SFRs are currently available in the literature, which enables a direct determination of the optical ICF for Ne and a comparison among abundances obtained from distinct methods, yielding a more reliable conclusion about the total Ne abundance.

The main goal of this paper is to examine the Ne abundance of SFRs, investigating the abundance discrepancy found by the use of different methods and obtaining a reliable ICF in the optical for this element. To do that, we compiled observed optical and infrared emission-line fluxes from the literature to derive the Ne ionic abundances. A photoionization model grid was also used in this analysis. The paper is organized as follows. In Section 2 we describe the observational data used along the paper and an analysis of the selected sample is performed. A description of the photoionization models is given in Sect. 3. The procedures to determine the ionic abundances are presented in Sect. 4. A comparison between neon ionic abundances obtained from distinct methods is given in Sect. 5. In Sect. 6 the ICFs computed for Ne^{++} and applied to the data set are presented. The conclusions of the outcomes are given in Sect. 7.

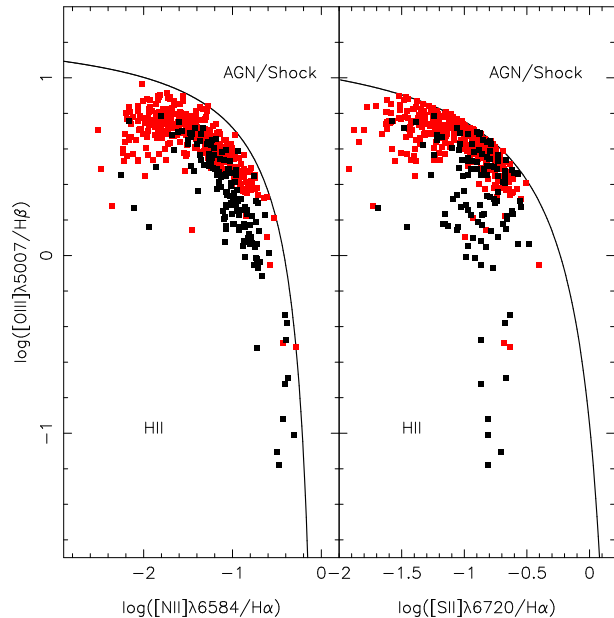


Figure 1. Diagnostic diagrams: $[\text{O III}]\lambda 5007/\text{H}\beta$ vs. $[\text{N II}]\lambda 6584/\text{H}\alpha$ (left) and $[\text{O III}]\lambda 5007/\text{H}\beta$ vs. $[\text{S II}](\lambda 6716+\lambda 6731)/\text{H}\alpha$ (right). Solid lines, taken from Kewley et al. (2006), separate objects ionized by massive stars from the ones containing active nuclei and/or shock excited gas as indicated. Black squares represent H II regions and red squares the ELGs compiled from the literature.

2 OBSERVATIONAL DATA

2.1 Sample description

Optical and infrared emission-line fluxes of a sample of emission-line galaxies (ELGs) – including H II galaxies (H II Gs), Wolf Rayet galaxies (WRGs), Blue Compact Galaxies (BCGs) and Dwarf Galaxies (DGs) – and H II regions (H II Rs) were compiled from the literature. Their emission-line intensities were already reddening corrected in the works from which we take the data. For most of the data this was done by using the ratio $\text{H}\alpha/\text{H}\beta$ and in some cases, where $\text{H}\alpha$ was not present in the spectra, the reddening coefficient was obtained from another hydrogen lines (e.g. data of Crockett et al. 2006).

The selection criterion was the presence of flux measurements of the optical $[\text{O II}]\lambda 3727$, $[\text{Ne III}]\lambda 3869$, $\text{H}\beta$, and $[\text{O III}]\lambda 5007$ emission-lines. We also compiled the line intensities of $[\text{O III}]\lambda 4363$, $\text{H}\alpha$, $[\text{N II}](\lambda 5755, \lambda 6548, \lambda 6584)$ and $[\text{S II}](\lambda 6717, \lambda 6731)$ when they were available. Regarding mid-infrared emission-lines, we selected 50 ELGs and 93 H II Rs located in the Magellanic Clouds, M 101, M 33 and M 83 whose $[\text{Ne II}]\lambda 12.81\mu\text{m}$ and $[\text{Ne III}]\lambda 15.56\mu\text{m}$ emission-lines were measured. The optical data were obtained by the use of long-slit, echelle and multi-object spectroscopy (MOS), while the infrared data were obtained with the *ISO* and *Spitzer Space Telescope*.

In the optical, we used the $[\text{O III}]\lambda 5007/\text{H}\beta$ vs. $[\text{N II}]\lambda 6584/\text{H}\alpha$ and $[\text{O III}]\lambda 5007/\text{H}\beta$ vs. $[\text{S II}](\lambda 6716+\lambda 6731)/\text{H}\alpha$ diagnostic diagrams (Figure 1) to distinguish objects ionized by massive stars from those containing an active galactic nucleus (AGN) and/or gas excited by shocks. To separate the dis-

tinct classes of objects, we used the criteria proposed by Kewley et al. (2006), where all objects with $\log[\text{O III}]\lambda 5007/\text{H}\beta < 0.61/[\log[\text{N II}]\lambda 6584/\text{H}\alpha - 0.05] + 1.3$ and $\log[\text{O III}]\lambda 5007/\text{H}\beta < 0.72/[\log[\text{S II}]\lambda(6717+\lambda 6731)/\text{H}\alpha - 0.32] + 1.3$ have massive stars as their main ionization mechanism. From this analysis we discarded 15 objects yielding a sample with 522 ELGs and 212 H II Rs.

Due to the non-homogeneity of the compiled data, we divided the sample into five groups according to the available emission-lines measured for each object:

- Group A - optical emission-lines, including the ones needed to directly estimate the electron temperatures and abundances.
- Group B - $[\text{O II}]\lambda 3727$, $[\text{Ne III}]\lambda 3869$, $\text{H}\beta$, $[\text{O III}]\lambda 5007$ (the optical selection criterion) and $[\text{O III}]\lambda 4363$.
- Group C - optical emission-lines except the ones sensitive to the temperature: $[\text{O III}]\lambda 4363$, $[\text{O II}]\lambda 7325$ and $[\text{N II}]\lambda 5755$.
- Group D - only the $[\text{O II}]\lambda 3727$, $[\text{Ne III}]\lambda 3869$, $\text{H}\beta$, and $[\text{O III}]\lambda 5007$ emission-lines (just fulfilling the optical selection criterion).
- Group E - the IR emission-lines.

Table 1 lists the bibliographic references of the sample, the number of objects taken from each work, their nature, the observational technique used during the data acquisition, and the group(s) to which the data belong. The objects in the A, B and E groups allow the computation of the ionic abundances and the ICFs from several methods used along the paper, while the ones in the C and D groups only enable a more accurate comparison between the data and the photoionization models to obtain a theoretical neon ICF.

To investigate the discrepancy between the neon ionic abundances from optical and infrared emission-lines, we selected the objects in our sample for which we can get a direct estimation of, at least, an electron temperature. They are those belonging to the optical groups A and B, and also to the IR group E. The sub-sample contains 23 objects and they are listed in Table 2 together with the corresponding optical and IR references. It is worth to emphasize that only for the objects in this sub-sample we can estimate the oxygen and neon ionic abundances via optical lines and the neon ones via infrared lines.

For the H II Rs located in the Magellanic Clouds, we converted the $\text{Br}\beta$ fluxes, directly measured from the observations by Vermeij & van der Hulst (2002), in $\text{H}\beta$ fluxes using the emissivities of Storey & Hummer (1995). We did not use the $\text{H}\alpha$ emission line at $10.52\ \mu\text{m}$, even though it is the closest hydrogen line to the mid-IR Ne ones, because for our compiled sample it is generally blended with an H_2 emission line. For the remaining sources we considered the observed $\text{H}\beta$ fluxes. A similar procedure was done by Wu et al. (2008) in their study of elemental abundances of BCGs using *Spitzer* observations.

2.2 Analysis of the sample

Along the years several authors have compiled spectroscopy data of star-forming regions from the literature in order to derive correlations between macroscopic properties of these objects (e.g. Pilyugin et al. 2004), or have suggested oxygen abundance calibrations using strong emission-lines (e.g.

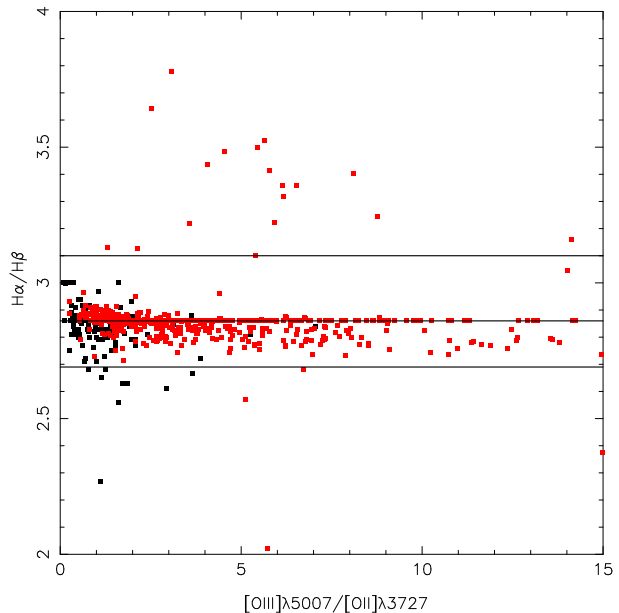


Figure 2. $\text{H}\alpha/\text{H}\beta$ vs. $[\text{O III}]\lambda 5007/[\text{O II}]\lambda 3727$. Black squares represent H II Rs and red squares the ELGs compiled from the literature. All data were reddening corrected in the works from which we taken the data. The lines represent the theoretical values for the low density recombination case B Balmer decrement $\text{H}\alpha/\text{H}\beta = 3.10$, 2.86 and 2.69 for temperatures of 5000, 10000 and 20000 K, respectively (Osterbrock 1989; Storey & Hummer 1995).

Pérez-Montero & Contini 2009; Nagao et al. 2006). However, the use of data sets obtained with different instrumentation and observational techniques, and including different objects such as whole galaxies, galaxy nuclei and individual H II Rs, i.e. non-homogeneous data, could lead to biased results. In what follows we investigate the possible sources of biases introduced in the present study due to the heterogeneity of our data set.

2.2.1 Aperture effects

Differences between the measurement apertures used in the optical and IR observations could contribute significantly to the discrepancies found between optical and IR abundance determinations (Vermeij & van der Hulst 2002) because many physical properties (e.g., stellar populations, metallicity, extinction) of galaxies vary with galactocentric radius (Moustakas & Kennicutt 2006a) or along nebulae (Oey et al. 2000). Kewley et al. (2005) presented a detailed analysis of the effect of aperture size on the star formation rate, metallicity, and reddening determinations for galaxies selected from the Nearby Field Galaxy Survey. They found that systematic and random errors from aperture effects can arise if fibers capture less than 20% of the galaxy light. Most of the SFRs in our sample can be treated as point sources and almost all the object extensions are observed, therefore, for these objects this effect is negligible. For the spatially resolved Magellanic H II Rs in our sample (see Table 2) this effect could play a more important role as was already pointed out by Vermeij & van der Hulst (2002). However, since our aim is to study the discrepancy found for the Ne^{++}

Table 1. Bibliographic references for the compiled sample.

ID	Reference	Object type	Number	Technique	Group
1	Lee et al. (2004)	KISS galaxies	13	long-slit	A
2	Vílchez & Iglesias-Páramo (2003)	DG	4	long-slit	A
3	Hägele et al. (2006)	H II G	3	long-slit	A
4	Hägele et al. (2008)	H II G	6	long-slit	A
5	Hägele et al. (2011)	H II G	2	long-slit	A
6	Skillman et al. (1989)	DG	2	long-slit	A
7	Thuan & Izotov (2005)	BCG	26	long-slit	B
8	Masegosa et al. (1994)	H II G	99	long-slit	A
9	Papaderos et al. (2008)	H II G	24	long-slit	A
10	Kobulnicky et al. (1999)	H II G	7	long-slit	A
11	Izotov et al. (2001)	BCG	2	long-slit	A
12	Izotov & Thuan (2004) ^a	BCG	33	long-slit	A
13	Izotov & Thuan (1998) ^a	BCG	17	long-slit	A
14	Izotov et al. (2006c) ^a	H II G	1	long-slit	A
15	Izotov et al. (1997) ^a	BCG	28	long-slit	A
16	Izotov et al. (1994) ^a	BCG	10	long-slit	A
17	Izotov et al. (2006b)	BCG	125	long-slit	A
18	Bergvall and Östlin (2002) ^a	BCG	3	long-slit	A
19	Guseva et al. (2000) ^a	WRG	8	long-slit	A
20	Guseva et al. (2011)	H II G	59	long-slit	A
21	Guseva et al. (2007) ^a	H II G	33	long-slit	B
22	López-Sánchez & Esteban (2009)	WRG	17	long-slit	A
23	Kobulnicky et al. (1997)	H II R	3	long-slit	A
24	Garnett et al. (1997)	H II R	7	long-slit	A
25	Kennicutt et al. (2003)	H II R	20	long-slit/echelle	A
26	van Zee et al. (1998)	H II R	58	long-slit	C
27	Vílchez et al. (1988)	H II R	4	long-slit	A, C
28	Kwitter & Aller (1981)	H II R	6	slit	A, C
29	Bresolin et al. (2009)	H II R	28	MOS	A, C
30	Lee & Skillman (2004)	H II R	15	long-slit	A, C
31	Bresolin et al. (2004)	H II R	8	MOS	C
32	McCall et al. (1985)	H II R	20	long-slit	A, C, D
33	van Zee (2000)	H II R	2	long-slit	A
34	Bresolin (2011)	H II R	19	MOS	D
35	Esteban et al. (2009)	H II R	9	long-slit	A, C
36	Crockett et al. (2006)	H II R	10	long-slit	B, D
37	Torres-Peimbert et al. (1989) ^a	H II R	3	long-slit	A, C
38	Engelbracht et al. (2008)	H II G	41	<i>Spitzer</i>	E
39	Wu et al. (2008)	BCG	9	<i>Spitzer</i>	E
40	Gordon et al. (2008)	H II R	7	<i>Spitzer</i>	E
41	Vermeij et al. (2002) ^a	H II R	7	<i>ISO</i>	A, C, E
42	Lebouteiller et al. (2008)	H II R	31	<i>Spitzer</i>	E
43	Rubin et al. (2008)	H II R	24	<i>Spitzer</i>	E
44	Rubin et al. (2007)	H II R	24	<i>Spitzer</i>	E

^a Papers from which the H β fluxes were obtained to compute neon ionic abundances.

ionic abundances and this ion is not expected to be formed in the extended low-surface brightness zones around SFRs, aperture effects neither represent an important factor.

2.2.2 Reddening correction

There are several ways to determine the reddening correction to be applied to the observed emission-line fluxes depending on the available information and the ad hoc assumptions. For example, the use of different ratios involving hydrogen emission-line fluxes, different extinction curves, and the use of a wide spectral range. All these facts could introduce some biases in our results. To investigate this effect, in Fig. 2 we plotted the H α /H β ratios against the ionization

degree parametrized by the [O III] λ 5007/[O III] λ 3727 ratio (e.g. Dors & Copetti 2003; Morisset et al. 2004) for the objects belonging to our sample. In this figure we can see very few points (\sim 3% ELGs and \sim 6% H II Rs) out of the range of the expected values of H α /H β ratio considering the theoretical values of Storey & Hummer (1995) for temperatures between 5000 and 20000 K, typical values of star-forming regions. Thus, we can conclude that differences in the reddening correction does not affect any statistical result obtained in this work.

Table 2. Objects with neon abundances determined via optical and infrared emission-line intensities.

Object	Reference ^a	
	Optical	Infrared
ELGs		
I Zw 18	15	38
Haro 11	18	38
UM 420	13	38
Mrk 1450	16	38
NGC 4861	15	38
UM 448	13	38
Mrk 930	13	38
Mrk 162	13	38
NGC1140	12	38
UM461	13	39
UM462	13	38
Tol2138-405	21	38
IIZw 40	19	38
SBS0335-052E	14	38
M 101 H II Rs		
NGC5455	37	40
NGC5461	37	40
NGC5471	37	40
Magellanic H II Rs		
N160A1	41	41
N160A2	41	41
N157B	41	41
N4A	41	41
N66	41	41
N81	41	41

^a The reference number is according to the ID listed in Table 1.

2.2.3 Instrumentation and observational techniques

The data compiled from the literature were acquired using different instrumentation and observational techniques. This may yield an additional scatter in the abundance determinations computed along this work that might lead to biased results. For example, if emission-lines with a broad component are present in low resolution spectra these could not be detected, and several physical properties obtained from these lines will be unreliable, such as abundance determinations (see Hägele et al. 2013, and references therein). Also, heavy elements abundance determinations from spectra with low signal-to-noise ratio can be overestimated (Wesson et al. 2012). However, discrepancies in emission-line ratios estimated for a given object observed using different techniques ranging from about 0.03 to 0.1 dex (Dors & Copetti 2005) translate into a few percent in the uncertainties of ionic abundance determinations. For example, if this discrepancy in the line ratio $[\text{O III}](\lambda 5007 + \lambda 4959) / \lambda 4363$ is 0.06 dex, the electron temperature derived using the different observations differs by about 400 K, yielding a $\log(\text{Ne}/\text{O})$ variation of about 0.1 dex. This value is of the order of the intrinsic scatter found for uniform samples studied using data obtained with the same instrumentation (see e.g. Kennicutt et al. 2003). When no systematic effects in the calibrations and data reduction exist, the physical properties derived using data obtained with different observational

techniques should be the same. For example, the physical parameters estimated for the star forming knots of Haro 15 are in very good agreement when derived using long-slit and echelle data (Hägele et al. 2012; López-Sánchez & Esteban 2009).

2.2.4 Nature of the sources

Our sample is composed by objects with different morphology and sizes, nevertheless they all have young and massive stellar clusters as their main ionization sources. The shape of the emission-line spectra of the objects in our sample is dominated by the ionizing fluxes from these massive stars. Therefore the same measurement and analysis techniques can be applied to derive the temperatures, densities and chemical composition of their interstellar gas (Hägele et al. 2006).

In general, the H II Rs and ELGs are located in the same zone in diagnostic diagrams (see e.g. Baldwin et al. 1981) implying that similar ionization mechanisms are taking place in these two different kind of objects (see Fig. 1). Other ionizing mechanisms could be present according to the evolutionary stages and the nature of the objects, such as galactic winds due to supernovae (e.g. Tang et al. 2007), contribution to the hydrogen emission fluxes by diffuse ionized gas (e.g. Oey et al. 2007; Moustakas & Kennicutt 2006; Calzetti et al. 2004), and/or the presence of obscured AGNs (Kewley et al. 2001), or even the effects of the presence of multiple kinematical components in the emission-line profiles (see e.g. Hägele et al. 2010; Firpo et al. 2010, 2011; Amorín et al. 2012, and references therein). The statistical contribution of these mechanisms is similar for the different kind of objects and they do not yield any bias on the physical conditions of the objects obtained in the present work.

3 PHOTOIONIZATION MODELS

To estimate the ICF for Ne via photoionization models, we compared the results of a grid of models performed using the Cloudy/8.0 code (Ferland et al. 1998) with the observational data sample. We used data of the groups A, B, C, D, and E which include all objects with optical and IR emission-lines available (i.e. 734 objects). The diagnostic diagrams $[\text{O III}]\lambda 5007 / [\text{O II}]\lambda 3727$ vs. $[\text{N II}]\lambda 6584 / [\text{O II}]\lambda 3727$, $[\text{Ne III}]\lambda 3869 / \text{H}\beta$ vs. $[\text{O II}]\lambda 3727 / \text{H}\beta$, $[\text{N II}]\lambda 6584 / \text{H}\alpha$ vs. $[\text{S II}]\lambda 6720 / \text{H}\alpha$, and $[\text{Ne III}]\lambda 5007 / [\text{Ne II}]\lambda 12.81\mu\text{m}$ vs. $[\text{O III}]\lambda 5007 / [\text{O II}]\lambda 3727$ were used for the comparison (see Fig. 3). The ICF values were obtained from the model results which better reproduce the observational data.

The model grid was built following the same procedures as Dors et al. (2011), with metallicities of $Z = 2.0, 1.0, 0.6, 0.4, 0.02, 0.01 Z_{\odot}$, and logarithm of the ionization parameter U from -3.5 to -1.5 dex with a step of -0.5 dex. For each model, the ionizing source was assumed to be a stellar cluster with a spectral energy distribution obtained from the stellar population synthesis code *Starburst99* (Leitherer et al. 1999), with an upper mass limit of $100 M_{\odot}$ and an age of 1 Myr. For the hypothetical nebula we adopted a constant electron density $N_e = 200$

cm^{-3} , plane-parallel geometry, and solar abundance ratio $\log(\text{Ne}/\text{O})=-0.61$ (oxygen from Allende Prieto et al. 2001 and Ne from Grevesse & Sauval 1998). In the models with $Z = 2 Z_{\odot}$, a value of $\log(\text{Ne}/\text{O})=-1.0$ was assumed, in order to fit the data in this high metallicity regime. This value is about the same found by Pérez-Montero et al. (2007) for very high metallicities. A complete description of the photoionization models is presented in Dors et al. (2011).

In Fig. 3 the diagnostic diagrams containing the observed emission-line intensities and the photoionization model results are shown. The typical errors of the observational emission-line ratios are about 10 per cent. It can be seen that the majority of the observational data falls within the regions occupied by the models when all the considered emission lines are in the optical range (see both upper and lower left panels). However, in lower right panel of Fig. 3, can be seen that the models produce lower values of the intensity line-ratio $[\text{Ne III}]15.56\mu\text{m}/[\text{Ne II}]12.81\mu\text{m}$. This problem was pointed out by Pérez-Montero & Vílchez (2009) and by Morisset et al. (2004). They found similar results from photoionization model grids built assuming different atmosphere models as photoionization sources. They concluded that this effect could not be due to uncertainties in stellar atmosphere models and must be due to problems in the atomic data of the mid-IR lines.

4 DETERMINATION OF IONIC ABUNDANCES

We considered two methods to determine the Ne^{++} , Ne^+ , O^+ , and O^{++} ionic abundances in our sample. The method that uses direct estimations of the electron temperatures (this method will be called the Visible-lines method) and the one that uses infrared emission-lines (this method will be called the IR-lines method).

4.1 Visible-lines method

For those objects with the appropriate optical emission-line measurements, we calculated the electron temperature (T_e) from the observed line-intensity ratio $R_{\text{O3}}=[\text{O III}](\lambda 4959 + \lambda 5007)/\lambda 4363$ for the high ionization zone (refereed as t_3). To do that we used the fitting function derived by Hägele et al. (2008) based on the TEMDEN routine of the nebular package of the IRAF¹ software:

$$t_3 = 0.8254 - 0.0002415R_{\text{O3}} + \frac{47.77}{R_{\text{O3}}}, \quad (1)$$

with t in units of 10^4K . The electron density (N_e) was computed from the ratio of $[\text{S II}]\lambda 6716/\lambda 6731$ using the TEMDEN routine and t_3 values given by the expression above.

The O^{++} and Ne^{++} abundances were computed using t_3 and following the relations given by Pérez-Montero et al. (2007):

$$12 + \log\left(\frac{\text{O}^{++}}{\text{H}^+}\right) = \log\left(\frac{I(4959) + I(5007)}{I(\text{H}\beta)}\right) + 6.144$$

$$+ \frac{1.251}{t_3} - 0.55 \log t_3 \quad (2)$$

and

$$12 + \log\left(\frac{\text{Ne}^{++}}{\text{H}^+}\right) = \log\left(\frac{I(3869)}{I(\text{H}\beta)}\right) + 6.486 + \frac{1.558}{t_3} - 0.504 \log t_3. \quad (3)$$

The O^+ ionic abundances were computed assuming $N_e = 100 \text{ cm}^{-3}$ and an electron temperature of the low ionization zone (refereed as t_2) derived from the theoretical relation:

$$t_2^{-1} = 0.693 t_3^{-1} + 0.281 \quad (4)$$

obtained from the models described by Pérez-Montero & Díaz (2003). Measurements of the $[\text{O II}]\lambda 7325$ auroral emission line, sensitive to the $[\text{O II}]$ electron temperature, are available for only 10-15 percent of our sample. Since we used the observational sample in a statistical way, we preferred to derive all the temperatures following the same procedure. Besides, almost all objects present high or moderate excitation degrees $[(I[\text{O III}]\lambda 4959 + \lambda 5007)/(I[\text{O II}]\lambda 3727 + I[\text{O III}]\lambda 4959 + \lambda 5007)] \geq 0.4$, as was defined by Pilyugin 2000]. Therefore the impact of O^+/H^+ variations to the total oxygen abundance and to the $\text{O}^{++}/(\text{O}^{++} + \text{O}^+)$ ratio (used in the neon ICF determinations) is small ($\approx 18\%$) in any case, and from a statistical point of view negligible. Only in those cases where the $[\text{O III}]\lambda 4363$ and $[\text{O II}]\lambda 7325$ auroral emission-lines were not available, we computed the O^+ ionic abundances assuming the electron temperature directly estimated from the observed line-intensity ratio $R_{\text{N2}}=[\text{N II}](\lambda 6548 + \lambda 6584)/\lambda 5755$:

$$t_2 = 0.537 - 0.000253R_{\text{N2}} + \frac{42.13}{R_{\text{N2}}} \quad (5)$$

fitting function given by Hägele et al. (2008). For few objects ($< 1\%$) t_2 was derived using this equation.

To derive the O^+ ionic abundances we used the expression given by Hägele and collaborators:

$$12 + \log\left(\frac{\text{O}^+}{\text{H}^+}\right) = \log\left(\frac{I(3727)}{I(\text{H}\beta)}\right) + 5.992 + \frac{1.583}{t_2} - 0.681 \log t_2 + \log(1 + 2.3n_e), \quad (6)$$

where $n_e = N_e/(10^4 \text{ cm}^{-3})$. As pointed out by these authors, the expressions given above are valid for temperatures from 7 000 to 23 000 K. The O^+ ionic abundances calculated using t_2 values from Eqs. 4 and 5 differ by about 0.2 dex. The data set used to determine the ionic abundances using this method belongs to groups A and B and is comprised by 579 objects ($\sim 80\%$ of the sample). All O^+ , O^{++} and Ne^{++} ionic abundances obtained via Visible method used along this study were computed from this data set.

4.2 IR-lines method

The Ne^+ and Ne^{++} ionic fractions can be determined using the intensities of the $[\text{Ne II}]\lambda 12.81\mu\text{m}$ and $[\text{Ne III}]\lambda 15.56\mu\text{m}$ emission-lines, respectively, and following a similar methodology to the one presented by Förster et al. (2001). The ionic abundance of an element can be given by

¹ Image Reduction and Analysis Facility, distributed by NOAO, operated by AURA, Inc., under agreement with NSF.

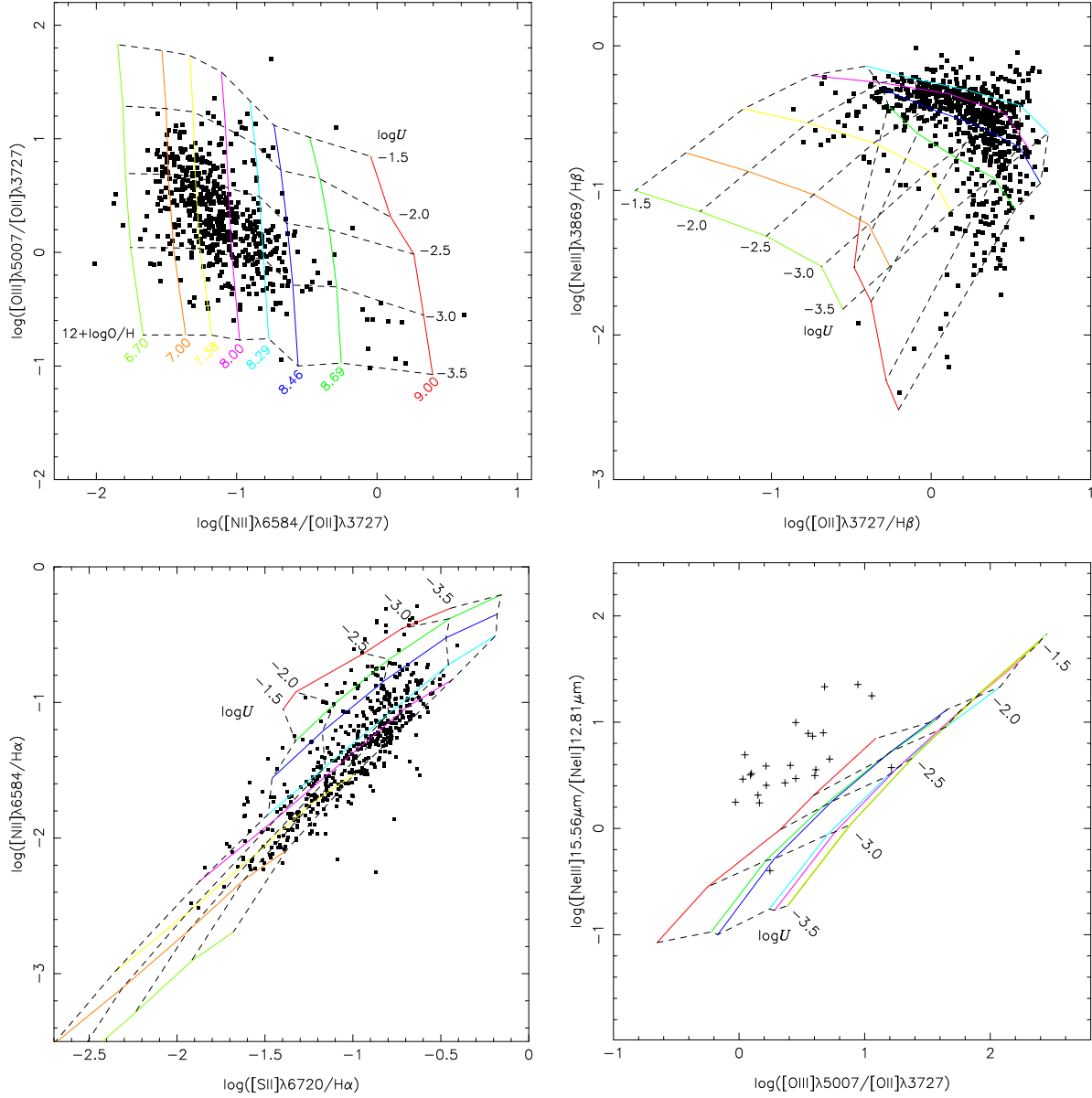


Figure 3. Diagnostic diagrams containing observational data taken from the literature (all groups) and the results of the grid of photoionization models described in this work. The solid lines connect curves of iso-(O/H), while the dashed lines connect curves of iso- U . The colour code for the values of the oxygen abundances (tracer of the metallicity) are the same in all panels and are indicated in the upper left panel. The solar oxygen abundance refers to Allende Prieto et al. (2001) and corresponds to $12+\log(\text{O}/\text{H})=8.69$. The values of $\log U$ are indicated in each panel. Points are the observational data. The typical errors (bars not shown) of the observational emission-line ratio are about 10 per cent.

$$\frac{n_{X^{+i}}}{n_{\text{H}^+}} = \frac{I_{\lambda}(X^{+i}) N_e j_{\lambda(\text{H}^+)}}{I_{\lambda}(\text{H}^+) N_e j_{\lambda(X^{+i})}}, \quad (7)$$

where $n_{X^{+i}}$ and n_{H^+} are the densities of the ions X^{+i} and H^+ , $I_{\lambda}(X^{+i})$ is intensity of a given emission-line emitted by X^{+i} , $I_{\lambda}(\text{H}^+)$ is the intensity of a reference hydrogen line, while $j_{\lambda(X^{+i})}$ and $j_{\lambda(\text{H}^+)}$ are the emissivity values given by the IONIC routine of the nebular package of the IRAF software which uses the Ne atomic parameters from Badnell et al. (2006), Griffin, et al. (2001), Kaufman & Sugar (1986), Butler & Zeppen (1994), and Mendoza (1983). These emissivity values are assumed to be constant in all abundance determinations because these

vary less than 5% over a large temperature range (see the pioneer work by Simpson 1975).

Using this method any error in the determination of these emissivities directly translates in a systematic shift in the derived Ne^+ and Ne^{++} ionic abundances. Taking into account all these assumptions we obtained

$$\frac{\text{Ne}^+}{\text{H}^+} = \frac{I(12.81\mu\text{m})}{I(\text{H}\beta)} \times 1.322 \cdot 10^{-4}, \quad (8)$$

and

$$\frac{\text{Ne}^{++}}{\text{H}^+} = \frac{I(15.56\mu\text{m})}{I(\text{H}\beta)} \times 6.323 \cdot 10^{-5}. \quad (9)$$

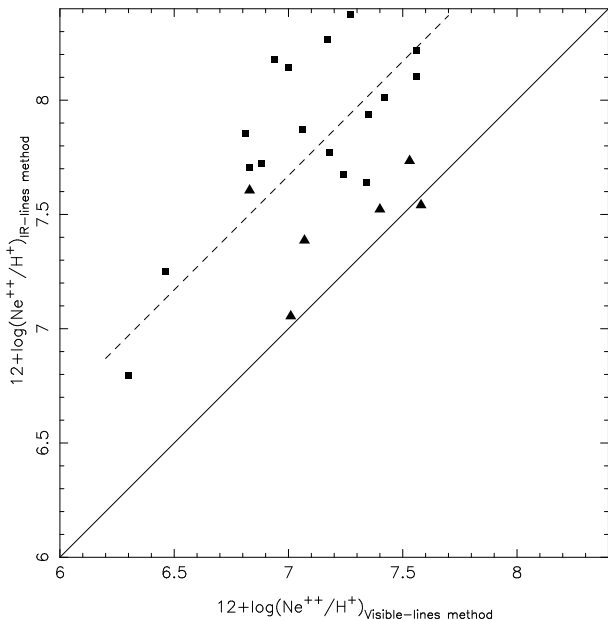


Figure 4. Comparison between ionic abundance of the $\text{Ne}^{++}/\text{H}^{+}$ derived using Visible-lines and IR-lines methods. Points represent estimations for the objects presented in Table 2, where squares are estimations using $\text{H}\beta$ fluxes and triangles the ones using $\text{Br}\beta$ fluxes. Solid line represents equality of the two estimates. Dashed line is the equality line shifted by the average of the differences between the ionic abundances. Typical errors in optical and infrared estimations are of about 15% and 10%, respectively (Vermeij & van der Hulst 2002).

5 COMPARISON OF NEON IONIC DETERMINATIONS

With the aim to compare the $\text{Ne}^{++}/\text{H}^{+}$ ionic abundances derived using the Visible-lines method and those using the IR-lines method, we plotted in Fig. 4 the results for the 23 objects listed in Table 2, the only ones for which we are able to apply both methods. These objects are those that simultaneously belong to groups A or B, and E. We can note a large discrepancy and scatter. Comparing the $\text{Ne}^{++}/\text{H}^{+}$ ionic abundance determinations obtained via the Visible-lines method with those based on the IR-lines method, we found discrepancies of about a factor of 4 in average, being $\text{Ne}^{++}/\text{H}^{+}$ underestimated when using the Visible-lines method (see Fig. 4).

The origin of this discrepancy is uncertain and several explanations have been proposed. Vermeij & van der Hulst (2002) compared optical and infrared ionic fractions obtained for a sample of HII regions located in the Magellanic Clouds. These authors found considerable discrepancies between determinations via these two methods, which were attributed to the difference in the area of the sky covered by the infrared and optical observations. However, as discussed above, aperture effects are not probably the origin of this huge discrepancy regarding a high-excitation ion as Ne^{++} .

Extinction might noticeably affect the comparison between the abundances obtained from IR and optical emission-lines. The blue optical $[\text{Ne III}]$ emission-line is more absorbed by dust than the mid-IR ones. Hence, if the nebular emission is highly reddened by dust the optical line does not trace all the Ne in the inner parts of the SFRs, yield-

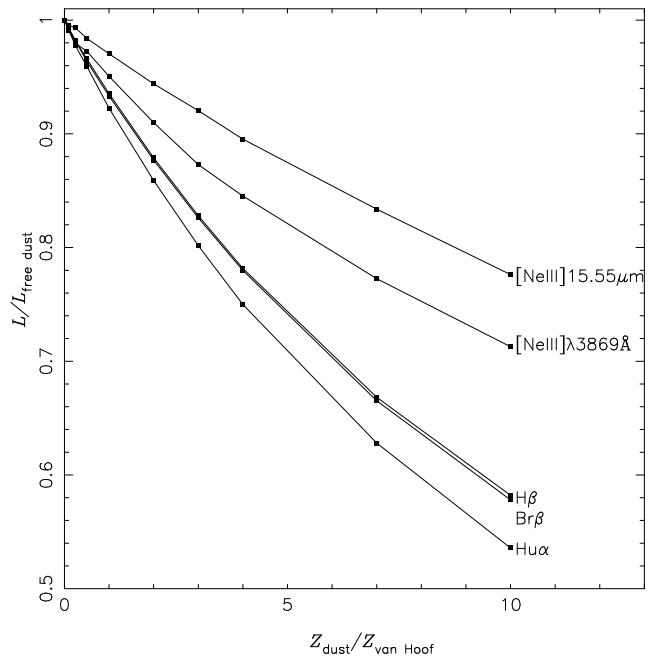


Figure 5. Logarithm of the luminosity predicted by our models for some hydrogen and neon emission-lines versus the dust internal abundance in relation to the default value assumed in the Cloudy code, i.e. $\log \text{O}/\text{H} \approx -4$. The grain model is described in van Hoof et al. (2001). Points are results for models considering different dust abundances connect by the curves. The results for different emission-lines are indicated. The $Z_{\text{dust}}/Z_{\text{van Hoof}}=0$ represents the models free of internal dust.

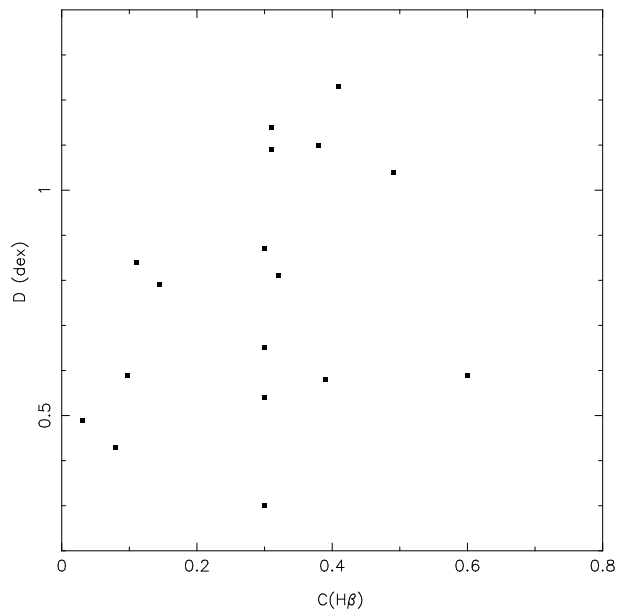


Figure 6. Differences between Ne^{++} ionic abundances obtained via the IR-lines and the Visible-lines methods as a function of the nebular reddening constant $C(\text{H}\beta)$ for the majority of the objects listed in Table 2.

ing an optical ionic abundance lower than that derived from the mid-IR lines. In the same way as for the Ne emission-lines, this effect could be enhanced by the use of $H\beta$ or $Br\beta$ emission lines instead of $H\alpha$ to derive ionic abundances in the mid-IR. In order to verify the extinction influence on the emission-lines, models with different internal dust abundance were built. In these, the only effect of grains on the continuous opacity was considered, i.e. the gas heating by grain emission was not considered in the calculations. The dust abundance was linearly scaled with the default value assumed in the Cloudy code, i.e. $\log O/H \approx -4$. The grain model is described in van Hoof et al. (2001). In Fig. 5 the predicted luminosity values ($L/L_{\text{free dust}}$) for some hydrogen and neon emission-lines in relation to the ones predicted by the model free of dust ($Z_{\text{dust}}/Z_{\text{van Hoof}}=0$) are shown. We can see that $H\beta$, $Br\beta$ and $H\alpha$ have about the same decreasing with the dust abundance, reaching $\sim 4\%$ maximum difference in their luminosities for $Z_{\text{dust}}/Z_{\text{van Hoof}}=10$. A similar behaviour is found for the neon emission-lines with a difference of about 6%. Even though these differences are within the observational measurement errors, we have used these predicted emission-line intensities to calculate the Ne^{++} abundance following the same procedure presented in Section 4. The largest difference found in Ne^{++} abundances derived from IR and the Visible methods was 0.3 dex. Therefore, this result shows that, at least, the extinction caused by the internal dust is not the main source of the neon ionic discrepancy.

To verify if there is an observational correlation between the extinction and the abundance discrepancy for the 23 objects listed in Table 2, we plotted in Fig. 6 the difference (D) between the Ne^{++} ionic abundances obtained via the IR-lines and the Visible-lines methods versus the nebular reddening constant $[C(H\beta)]$ compiled from the literature and used by the authors to correct their observational data. There is no evident correlation between the discrepancy and the extinction found from the Balmer decrement.

For five objects of our sample: N81, N4A, N66, N160A1, and N160A2, both $Br\beta$ and $H\beta$ fluxes were obtained directly from spectroscopy observations by Vermeij et al. (2002), Dufour & Harlow (1977a,b) and Heydari-Malayeri et al. (1998, 2002). We use these data and the $[Ne III]15.55\mu m$ from Vermeij et al. (2002) to calculate Ne^{++}/H^+ ionic abundances of these objects using both hydrogen lines. We found neon ionic estimations in agreement by about 0.2 dex, indicating that dust absorption is not the main source of the discrepancy, at least for these objects. Another observational support to this result arises from the data presented by Wu et al. (2008). These authors pointed out that most of the galaxies observed by them, which include 50% of the ELGs presented in Table 2, do not show a strong $9.7\mu m$ silicate feature and, consequently, have low dust extinction. Moreover, as noted in Fig. 4, for the objects whose both $Br\beta$ and $H\beta$ fluxes were measured, the ionic difference is also found, indicating that the differential absorption of optical and infrared emission lines is not the main cause of the discrepancy. Thus, we can assume that this effect is negligible for these objects.

As can be seen in Sect. 3, and was already noticed by Pérez-Montero & Vílchez (2009) and Morisset et al. (2004), the photoionization models can not reproduce diagnostic diagrams based on Ne mid-IR lines independently of the used

stellar atmospheres. Therefore, this could be symptomatic of inaccurate atomic data involving these emission-lines and can be on the basis of the found discrepancies when deriving abundances from optical and mid-IR emission lines. In particular, the atomic parameter which can affect the abundance determinations is the collision strength for the $[Ne III]\lambda 15.56\mu m$ emission-line. However, it is not probable that uncertainties in this parameter be the main cause of the discrepancy found in our study. Along the years differences in neon collision strength have been found. For example, the collision strength for $[Ne III] 3P_1 \rightarrow 3P_2$ derived by Blaha (1969) is $\Omega=0.581$. The Ω values derived in the IRON project by Butler & Zeippen (1994) range from 0.481 to 0.778 for temperatures ranging from 10^3 to 10^5 K. Later computations by McLaughlin & Bell (2000) yield a lower Ω value by about a 20% than the one proposed by Blaha (1969). Recently, McLaughlin et al. (2011) have recomputed the collision strengths for some neon lines using a small scale 56-level Breit-Pauli calculation and a large-scale 554-levels R-matrix Intermediate Coupling Frame Transformation (ICFT). They showed that different Ω values are obtained by the use of these suppositions, in the sense that for 56-level Breit-Pauli calculation Ω ranges from about 0.5 to 1.0 and for the 554-levels ICFT ranges from about 0.4 to 0.8. It must be noted that these results are in good agreement with earlier derivations. Nevertheless, even assuming that the collision strength for the $[Ne III]\lambda 15.56\mu m$ emission-line can vary by a factor of two, it is not enough to conciliate the ionic abundance discrepancy.

Finally, another supposition is the presence of electron temperature fluctuation amplitude inside the ionized gas. It can lead to an underestimation of the ionic abundances obtained via optical collisionally-excited lines when these fluctuations are not considered since these lines are strongly dependent on the electron temperature (see e.g. Peimbert 1967, 2003; Krabbe & Copetti 2005). This problem can be alleviated using abundances based on IR emission-lines, whose fine-structure transitions have a weak dependence on the electron temperature (e.g. Dinerstein et al. 1985; Rubin et al. 2001; Nolleberg et al. 2002; Garnett et al. 2004). Since the electron temperatures are related with the chemical composition of the emitting gas, temperature fluctuations are essentially equivalent to abundance variations across the nebula (Kingdon & Ferland 1998).

To test the effect of the presence of temperature fluctuations and/or abundance variations, we built a grid of photoionization models using Cloudy. These models are similar to the ones described in Sect. 3 and presented in Fig. 3 but considering the presence of chemical inhomogeneities in the theoretical nebula and spherical geometry. The plane-parallel geometry assumed in the later models can not be used to test variations along the radius of the hypothetical nebulae, since makes the inner radius much larger than the thickness of the cloud and the results about independent on electron temperature fluctuation amplitude. In this case we considered a nebula with $Z = Z_{\odot}$, with an inner radius of 4 pc and an outer radius where the temperature falls below 4000 K (≈ 30 pc), and a number of hydrogen-ionizing photons emitted by the ionizing star cluster of $10^{50} s^{-1}$. It was assumed that the metallicity varies along the radius of the nebula as a sine wave, with period P ranging from 0.01 to 2 pc, including 0.01, 0.1, 0.25, 0.5 and 1 pc. Also a model

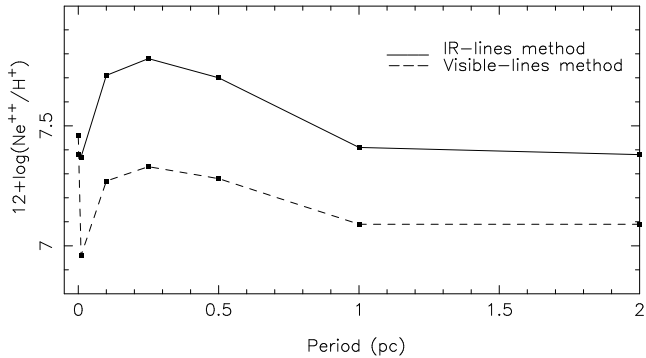


Figure 7. Results of photoionization models considering abundance variations along the radius of the nebula. $\text{Ne}^{++}/\text{H}^{+}$ ionic abundances obtained via the Visible-lines and the IR-lines methods (dashed- and solid-lines, respectively) as a function of the period P of the abundance variations.

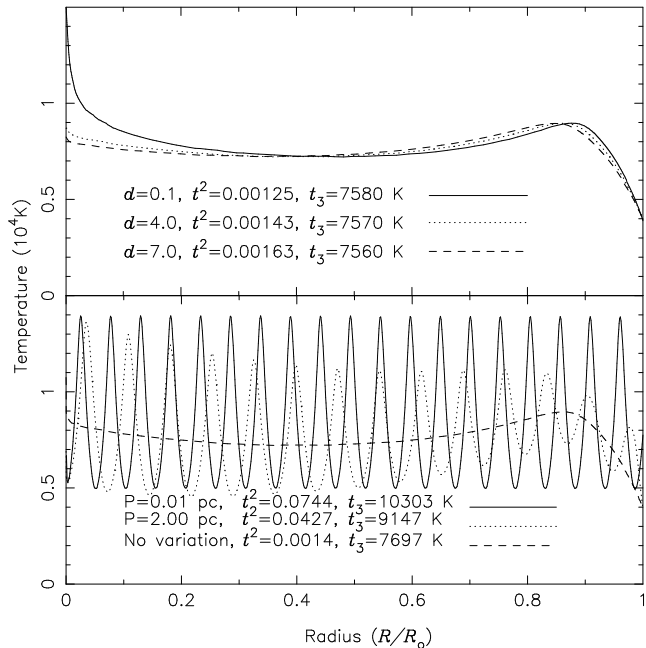


Figure 8. Temperature structure of the theoretical nebula from our photoionization models. For each model, R/R_0 is the radius normalized to the outermost one (R_0). Bottom panel: The curves represent result models with different values of P (period of the sine wave which the metallicity varies along the radius of the nebula) as indicated. Top Panel: The curves represent model results with no abundance variations but with different distances between the central ionizing source and the inner face of the gas, represented by d , as indicated. The t^2 as defined by Peimbert (1967) and the electron temperature t_3 for each models are shown.

with no variations and solar abundance was considered. We considered a set of models with an abundance amplitude of 0.8 dex, which takes metallicity values between $2 \times Z_{\odot}$ and $0.3 \times Z_{\odot}$. Kingdon & Ferland (1995) built grids of photoionization models using similar sine wave variations but applied to the total hydrogen density across the nebula.

We used the emission-line intensities given by our models for each value of P to calculate the $\text{Ne}^{++}/\text{H}^{+}$ ionic abundances applying the Visible-lines and the IR-lines methods following the same procedure as described in Section 4.

Thus, we obtain two estimations of $\text{Ne}^{++}/\text{H}^{+}$ for each model. Fig. 7 shows these estimated values of $\text{Ne}^{++}/\text{H}^{+}$ plotted as a function of the period P of the abundance variations. As it can be seen when no variations are considered, the $\text{Ne}^{++}/\text{H}^{+}$ ionic abundances estimated by each method differ by less than 0.1 dex, which is within the errors of the methods. When abundance variations are present the differences could reach about 0.5 dex, being the ionic abundances via the IR-lines method the largest one. This value is very similar to the one found in Fig. 4 between the estimated Ne ionic abundances derived applying the Visible-lines and the IR-lines methods to the observational data. Moreover, these differences, as expected, depend on the metallicity amplitude of the models, increasing (decreasing) with an increment (decrement) in the amplitude (models not shown). Therefore, the temperature fluctuations studied through the abundance variations across the nebula could be a probable explanation for the discrepancy between the estimated Ne abundances by these two methods. In Fig. 8 (bottom panel), we have plotted the temperature structure² of our models with $P=2$, 0.01 and no fluctuations versus the radius normalized to the outermost one. In this figure we also show, for each P , the values of the temperature fluctuation parameter (t^2) as defined by Peimbert (1967) and the electron temperature t_3 using the predicted values of R_{O3} and the Eq. 1.

We found, as expected, that abundance variations translates into temperature fluctuations. As can be seen in Fig. 8, t_3 decreases when larger values of P are assumed, however, the average temperature weighted by the electron density over the volume of the nebula $\langle T \rangle$ (not shown), as defined by Peimbert (1967), is about constant with P . The model with $P=0.01$ pc shows a constant temperature fluctuation amplitude of about 9000 K, while the amplitude showed by the model with $P=2$ decreases with the radius. Interestingly, the t^2 value, when no fluctuations are considered, is about the same found in some H II Rs (see e.g. Krabbe & Copetti 2002) and H II Gs (e.g. Hägele et al. 2006). On the other hand, the t^2 values that explain the differences found when comparing ionic abundances obtained via recombination and collisional excited emission-lines (see e.g. Peimbert 2003; García-Rojas et al. 2006) are in good agreement with those given by the models with P different than zero. A more detailed study about spatial electron temperature fluctuations in ionized nebulae from photoionization models is given by Copetti (2006).

Along decades observations have failed in found a direct evidence of chemical inhomogeneities in H II regions (e.g. Oliveira et al. 2008; Lebouteiller et al. 2008; García-Rojas et al. 2006; Krabbe & Copetti 2002) and in planetary nebulae (e.g. Krabbe & Copetti 2005; Rubin et al. 2002; Liu et al. 2000). Thus, an another source of temperature fluctuations can be the presence of density variations in the gas. Rubin (1989) showed that large-scale variations in electron density in the gas do arise electron

² In Cloudy code the nebula is divided in concentric zones with physical conditions across them about constant. This causes the zone number in each computed model to vary. The electron temperatures of these zones are shown in Fig. 8. See Cloudy manual for more details.

temperature fluctuations. Considering the H II region models of Rubin (1985), this author pointed out that if N_e varies by a factor of about 10, the electron temperature can range up to 2000 K (see also Kingdon & Ferland 1995). Recently, Mesa-Delgado et al. (2012) presented results from integral field spectroscopy of a region near to the Trapezium Cluster and found the presence of high-density gas ($N_e \approx 4 \times 10^5 \text{ cm}^{-3}$), which are much higher than the typical values obtained either for galactic and extragalactic regions (see Copetti et al. 2000). Unfortunately, a larger number of observations, such as the ones by Mesa-Delgado et al. (2012), are needed to confirm the high scale density fluctuations in ionized nebulae.

Another likely reason for the presence temperature fluctuations are different proximities of gas to the ionizing O stars, since these are mainly responsible for the ionization structure. To test this, we built models considering different distances, d , between the central ionizing source and the inner face of the gas, where d ranged from 0.1 to 7 pc. These values are consistent with the ones used by Simpson et al. (1997) in a study of the Galactic H II region G0.18-0.04. Again, the predicted emission-lines were used to calculate the $\text{Ne}^{++}/\text{H}^+$ ionic abundances applying the Visible-lines and the IR-lines methods, following the same procedure as described in Section 4. We found a 0.0-0.2 dex difference in $\text{Ne}^{++}/\text{H}^+$. In Fig. 8 (top panel) the temperature structure of the models is shown. We can note a hot region very near the central star, however, this region is too small to affect the derived abundances, since no significant changes among the models neither in the t^2 nor in t_3 values are obtained. Models with a more complicated geometry, with many stars distributed through the gas (e.g. Ercolano et al. 2007), might cause the temperature variations and consequently help to explain $\text{Ne}^{++}/\text{H}^+$ ionic discrepancies.

6 NEON ICFs

6.1 ICFs determinations

The ICFs stand for the unseen ionization stages of each element. For the Ne^{++} it is defined as

$$\text{ICF}(\text{Ne}^{++}) = \text{Ne}/\text{Ne}^{++}. \quad (10)$$

The ICF for Ne^{++} can be directly computed using only $[\text{Ne II}]_{12.81\mu\text{m}}$ and $[\text{Ne III}]_{15.56\mu\text{m}}$ emission-line fluxes. Assuming that the total Ne abundance is

$$\frac{\text{Ne}}{\text{H}} \approx \frac{\text{Ne}^+}{\text{H}^+} + \frac{\text{Ne}^{++}}{\text{H}^+}, \quad (11)$$

and using Eq. 10 we obtained

$$\text{ICF}(\text{Ne}^{++}) = 1 + \frac{\text{Ne}^+}{\text{Ne}^{++}}. \quad (12)$$

Using Eqs. 8 and 9, we found

$$\text{ICF}(\text{Ne}^{++}) = 1 + 2.10 \times \frac{F_{[\text{Ne II}]\lambda 12.81\mu\text{m}}}{F_{[\text{Ne III}]\lambda 15.56\mu\text{m}}}. \quad (13)$$

Therefore to estimate the Ne ICF using the IR lines it is not necessary the use of hydrogen emission-line fluxes. Thus, we were able to use all the objects belonging to group E (143 objects). A histogram containing the ICF values lower than 10 is shown in Fig. 9. It can be seen that almost all the ICF

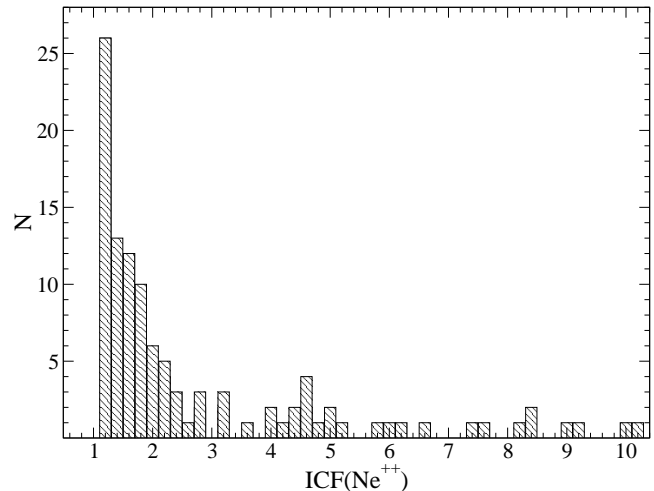


Figure 9. Histogram containing the values of the $\text{ICF}(\text{Ne}^{++})$ obtained using the IR emission-line intensities and Eq. 13 for the objects belonging to the group E and with ICF values lower than 10.

values ($\approx 85\%$) are lower than 5. Very high values (> 10) are also found. The objects that present the largest ICF values are IC342 (≈ 257), NGC 5236 and NGC 5253 (≈ 58), Searle 5 (≈ 55), NGC 3628 (≈ 45), and NGC 2903 (≈ 32). Also high ICFs were obtained from data of some H II Rs in M 83 observed by Rubin et al. (2007). These values (not shown) could reflect the presence of cool ionizing sources in these objects.

A classical way to determine the neon ICF takes advantage of its relation with the ionic oxygen $\text{O}^{++}/(\text{O}^+ + \text{O}^{++})$ ratio. From a fit in our photoionized model results presented in Sect. 3 we obtained:

$$\text{ICF}(\text{Ne}^{++})_{\text{model}} = 0.741 - 0.08x + \frac{0.393}{x}, \quad (14)$$

where $x = \text{O}^{++}/(\text{O}^+ + \text{O}^{++})$. This relation is shown in Fig. 10. In this figure are also shown the ICFs obtained using photoionization models by Pérez-Montero et al. (2007) and by Izotov et al. (2006b), the classical approximation $[\text{ICF}(\text{Ne}^{++}) = \text{O}/\text{O}^{++}]$ which the ionic abundances were derived from Visible-lines method and using our data sample, and the ICFs obtained from the IR-lines method.

Fitting the results obtained using the ICF via IR-lines method and x via Visible-lines method, represented by points in Fig. 10, we obtained the following expression:

$$\text{ICF}(\text{Ne}^{++})_{\text{IR}} = 2.382 - 1.301x + \frac{0.05}{x}, \quad (15)$$

valid for $x \geq 0.4$. Unfortunately, only for 23 objects in our sample we have measurements of the Ne infrared emission-line intensities and we were able to determine the $\text{O}^{++}/(\text{O}^+ + \text{O}^{++})$ ratio via the Visible-lines method (see Fig. 10). It must be noted that this sample comprehends objects in a large range of metallicity ($7.1 < 12 + \log(\text{O}/\text{H}) < 8.50$ dex) as well as a large range of ionization degree ($0.4 < \text{O}^{++}/(\text{O}^+ + \text{O}^{++}) < 1.0$).

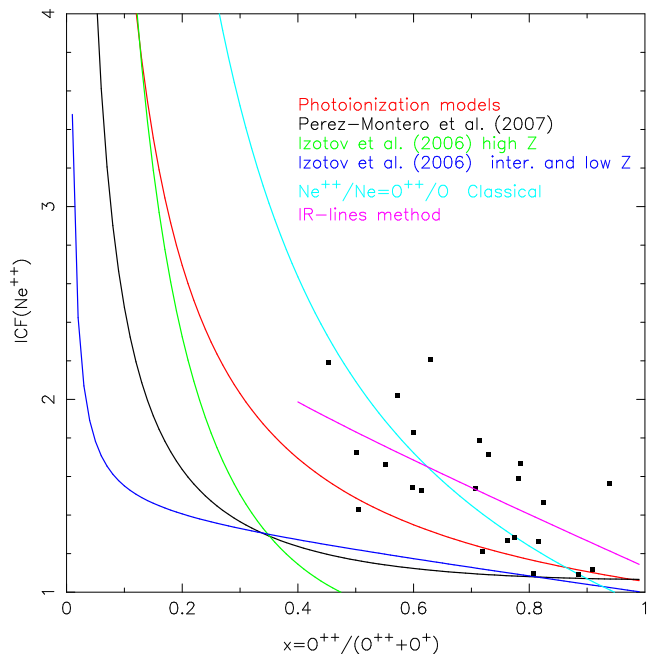


Figure 10. Relation between $\text{ICF}(\text{Ne}^{++})$ and $x = \text{O}^{++} / (\text{O}^{++} + \text{O}^{+})$ ionic abundance ratio. Solid lines correspond to our fittings to the ICF for Ne and those found by different authors as indicated. Points represent the data whose ICFs were determined via IR-lines method and listed in Table 2.

6.2 Application of the Neon ICFs

To test the differences in Ne/H total abundance yielded by the use of different ICFs, we used the observational data to compute $\text{Ne}^{++}/\text{H}^{+}$ ionic abundances via the Visible-lines method and applied different ICFs to obtain the Ne total abundances. Fig. 11 shows the comparisons between the Ne/H derived using the ICF from the IR-lines method (Eq. 15) and those values estimated applying the ICFs derived by: (a) Pérez-Montero et al. (2007), (b) Izotov et al. (2006b), (c) photoionization models (Eq. 14) described in this work, and (d) the classical approximation [$\text{ICF}(\text{Ne}^{++}) = \text{O}/\text{O}^{++}$]. It can be seen that, in general, the expression from the IR-lines method gives higher ICF values, and consequently higher Ne/H values, by about 0.08-0.13 dex than those obtained using ICFs from Pérez-Montero et al. (2007), Izotov et al. (2006b), and from our photoionization models. For low-excitation objects, we find that the high metallicity models by Izotov et al. (2006b) are in agreement with our theoretical relation. Finally, the classical ICF approximation yields Ne/H values in consonance with the ICFs via the IR-lines method.

6.3 Ne/O vs. O/H

A very important issue is the study of the relation between the Ne/O ratio and the total oxygen abundance, for which there is not a consensus. Wang & Liu (2008), using oxygen and neon abundances of a sample of planetary nebulae and H II RRs, found that the Ne/O ratio increases with O/H in both types of nebulae. A similar result was found by Guseva et al. (2011) and Izotov et al. (2006b) for a large sample of low-metallicity

ELGs. Pérez-Montero et al. (2007), using a photoionization model grid to derive the Ne ICF found, for a large sample of SFRs, that the Ne/O behaviour agrees with the assumption of a constant value for the low metallicity regime ($12 + \log(\text{O}/\text{H}) < 8.2$) but shows a slightly decrease for the high metallicity regime ($12 + \log(\text{O}/\text{H}) > 8.2$). Moreover, Willner & Nelson-Patel (2002), using mid-IR derivations of the neon abundances of a sample of H II RRs located in M 33, obtained a flat neon abundance gradient as a function of the galactocentric radius, as well as a decrement of the Ne/O ratio when the O/H increases.

To investigate this issue, we applied the different ICFs for Ne shown in Fig. 10 to the ionic Ne^{++} abundances estimated using the Visible-lines method to obtain total Ne abundances for the compiled sample. We then combined these values with the total oxygen abundances to estimate Ne/O ratio. Figs. 12 and 13 show these values as a function of $12 + \log(\text{O}/\text{H})$ for our ICFs and those from the literature, respectively. In these figures we also show the logarithm of the average Ne/O value derived using the different ICFs, and their standard deviations. These average values are consistent in all the cases with the adopted solar one. From a visual inspection of the distributions of our observational sample in these diagrams, can be seen that there is a flat relation between the logarithms of the Ne/O and the O/H ratios for the whole studied metallicity range, from about 7 to 8.5 dex. We also perform a fitting to these data assuming a linear regression with slope a and the regression constant b , and without taking into account the individual errors. In Table 3 we list the coefficients of the fittings. We obtain null, positive and negative slopes for the different ICFs. However, in all the cases these slopes are close to zero. In the worst case, $a = -0.08$, a metallicity variation equal to the complete metallicity range (1.5 dex, equivalent to a factor of about 32) implies a variation of the Ne/O ratio equal to 0.12 dex (equivalent to a factor of about 1.3). This Ne/O variation is very similar to the standard deviation of the data. We also analysed the statistical dependence of Ne/O with O/H using the Spearman's rank correlation on the data, finding that the Ne/O is statistically constant independently of the metallicity value. Another test was done considering different metallicity regimes. We computed the average Ne/O value for the high ($12 + \log(\text{O}/\text{H}) > 8.2$) and the low ($12 + \log(\text{O}/\text{H}) < 8.2$) metallicity regime for each considered ICF. In Table 3 these results are listed. None variation of the Ne/O with O/H is noted for these different regimes and for each ICF. Therefore, we can conclude that the Ne/O and the metallicity have a flat relation for this sample. This flat Ne/O vs. O/H behaviour for the whole range of O/H analysed is a robust test of nucleosynthesis prediction and supports a very limited (if any) oxygen depletion in dust. The oxygen abundances in grains are poorly known. For example, Izotov et al. (2006b) interpreted that the slight increase of Ne/O with the metallicity is due to depletion of about 20% of O onto grains. Also, Peimbert & Peimbert (2010) found an increasing depletion of O atoms of about 0.1 dex with increasing O/H for three objects in a large range of metallicity. From our data we derived a dispersion of Ne/O for a fixed O/H value of ~ 0.10 dex. Therefore, none conclusion can be obtained about the oxygen depletion on dust.

On the other hand, it must be noted that the scatter of the Ne/O increases with the metallicity, showing the

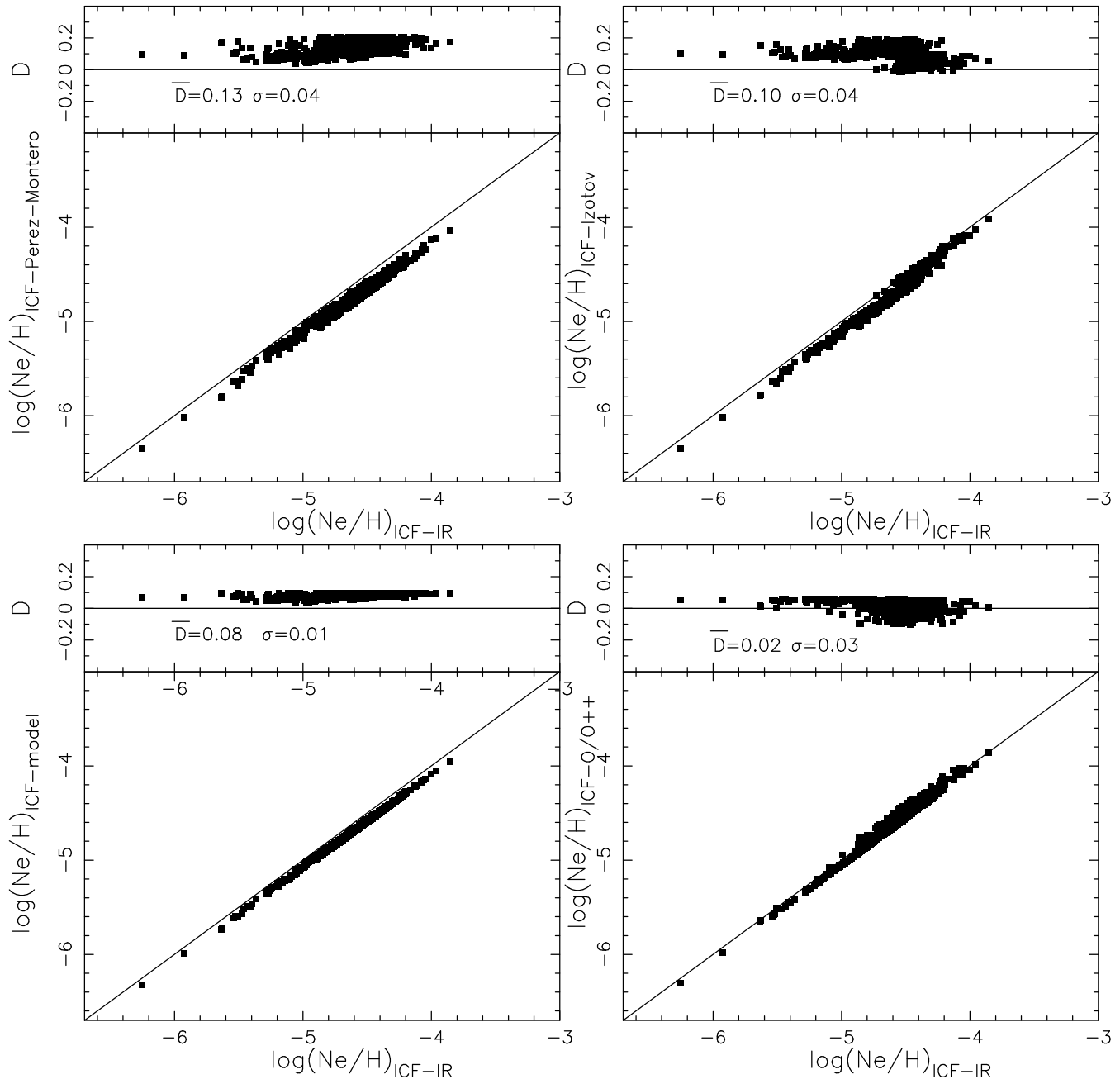


Figure 11. Comparison between total Ne/H abundances obtained from the $\text{Ne}^{++}/\text{H}^{+}$ ionic ones using the Visible-lines method and applying different ICFs as indicated. Points represent estimations for the objects belonging to the groups A and B. The top panel of each diagram shows the difference between the estimations using the methods considered. The average value \bar{D} of this difference and the dispersion are shown in each plot. Solid lines represent equality of the two estimates.

distribution of the data a triangular-like shape. This result was also found by Kennicutt et al. (2003) for H II R in M101, NGC 2403 and dwarf irregular galaxies. They argued that this effect can reflect high sensitivity to the local radiation field as Ne^{++} and O^{++} become minor constituents of the nebular material when the O^{+}/O increases, which is equivalent to a metallicity increment. As the metallicity of the gas material increases the electron temperature decreases, thus, the Ne^{++} and O^{++} emission-line intensities becomes weak. Therefore, the increment of scatter going to the higher abundances should be a normal behaviour admit-

ting that errors in the measurements of the sensitive lines are found to be larger (statistically) for higher abundance H II R. In fact the triangular shape mentioned is probably just a product of this. We have also tested the dependence of Ne/O on the temperature fluctuations, since neon and oxygen have slightly different temperature coefficients. Using the earlier result models and computing Ne/H and O/H following the same procedure described in Sect. 4, we found that $\log(\text{Ne}/\text{O})$ is -0.53 and -0.36 for $P=0.0$ and 0.01 , respectively. Thus, temperature fluctuations would not be a source of systematic errors in the Ne/O derivation.

Table 3. Coefficients of the linear regressions $\log(\text{Ne}/\text{O})=a \times [12+\log(\text{O}/\text{H})]+b$ fitted to data plotted in Figs. 12 and 13. Columns 2 and 3 list the slope and the constant coefficient, respectively, together with their formal errors. Columns 4 and 5 are the mean values of the $\log(\text{Ne}/\text{O})$ for the high and low metallicity regimes considered.

ICF(Ne ⁺⁺)	<i>a</i>	<i>b</i>	$\log(\langle\text{Ne}/\text{O}\rangle)$	
			high <i>Z</i>	low <i>Z</i>
IR-lines method	+0.02 ± 0.01	-0.77 ± 0.11	-0.63 ± 0.11	-0.62 ± 0.08
Photoionization models	-0.02 ± 0.01	-0.53 ± 0.10	-0.74 ± 0.13	-0.70 ± 0.09
Izotov et al. (2006b)	+0.06 ± 0.01	-1.17 ± 0.12	-0.70 ± 0.12	-0.75 ± 0.10
Pérez-Montero	-0.08 ± 0.01	-0.08 ± 0.14	-0.83 ± 0.13	-0.75 ± 0.13
ICF(Ne ⁺⁺)=O/O ⁺⁺	+0.04 ± 0.01	-1.06 ± 0.12	-0.64 ± 0.11	-0.65 ± 0.09

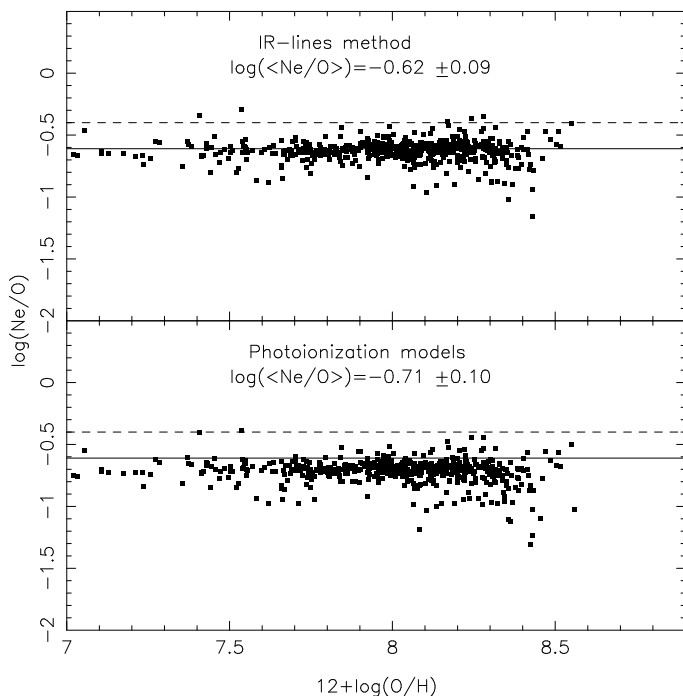


Figure 12. Relation between $\log(\text{Ne}/\text{O})$ and O/H using the Visible-lines method and our two different $\text{ICF}(\text{Ne}^{++})$ as indicated. Points represent estimations for the objects belonging to the groups A and B. The solid line represents the Ne/O abundance ratio derived using the oxygen abundance from Allende Prieto et al. (2001) and the neon from Grevesse & Sauval (1998), while the dashed line represents the value derived by Drake & Testa (2005) using *Chandra* X-ray spectra of a sample of nearby solar-like stars. The average and the standard deviation of $\log(\text{Ne}/\text{O})$ taking into account low and high metallicity regimes are shown in each plot.

Finally, we tested the Ne/O dependence on the ionization degree $x=\text{O}^{++}/(\text{O}^{+} + \text{O}^{++})$. To do that, we used the compiled sample to obtain the Ne/O abundances via Visible-lines method and the x values. The ICF for Ne from IR-lines method (Eq. 15) was considered. In Fig. 14 (bottom panel) we can see that higher Ne/O values are found for objects with high excitation. This result is independent of the ICF considered. Although the neon ICF and O/H ratio decrease with x , the behaviour of the Ne/O ratio is due to the increment in the $\text{Ne}^{++}/\text{H}^{+}$ with x , as can be seen in Fig. 14 (top panel).

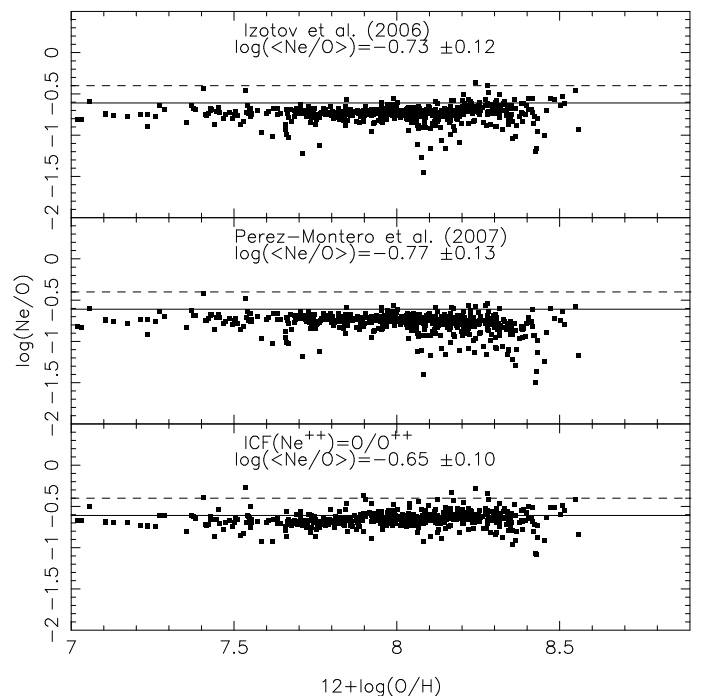


Figure 13. As Fig. 12 for the $\text{ICF}(\text{Ne}^{++})$ from the literature as indicated.

7 CONCLUSIONS

In this work we show that the ionic fractions $\text{Ne}^{++}/\text{H}^{+}$ obtained via optical direct detections of the electron temperature are underestimated by about a factor of 4 in relation to those estimated via mid-infrared emission-lines. We discussed several possible causes responsible of this discrepancy, including:

(i) Different apertures between optical and mid-IR observations, as was already suggested by Vermeij & van der Hulst (2002). This effect should not be of great importance for the most part of the analysed sample, which behaves as point-like sources. Besides, this effect has minimum effect in a high-excitation ion such as Ne^{++} .

(ii) Differential extinction effects. Mid-IR emission-lines are possibly tracing a deeper ionization structure than optical ones. Besides, due to no reliable measurements of the $\text{H}\alpha$ hydrogen recombination line at $10.52 \mu\text{m}$ since it is blended with an H_2 line, ionic abundances were derived in relation to $\text{H}\beta$ or $\text{Br}\beta$ emission-lines. We did not find any

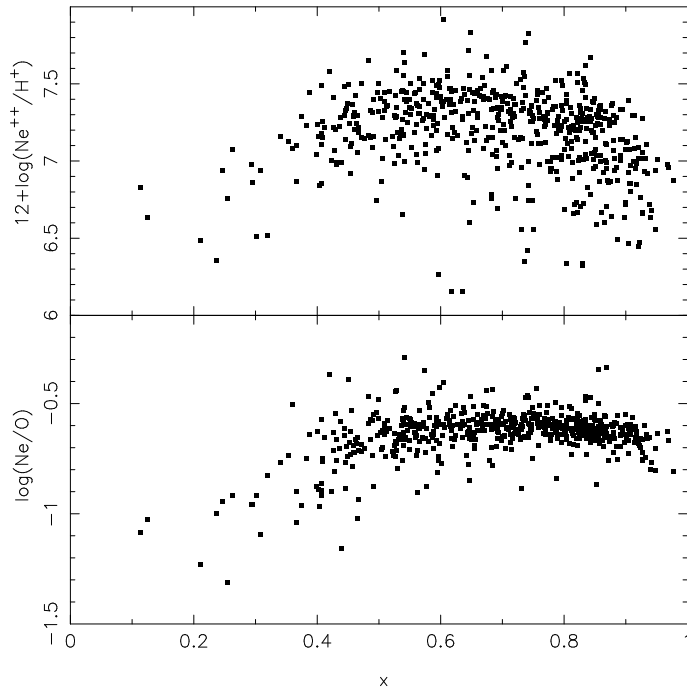


Figure 14. Bottom panel: Relation between $\log(\text{Ne}/\text{O})$ and the ionization degree $x = \text{O}^{++}/(\text{O}^+ + \text{O}^{++})$ obtained using the Visible-lines method, the compiled sample and the ICF for Ne from the IR-lines method. Points represent estimations for the objects belonging to the groups A and B. Top panel: Relation between estimations of $12 + \log(\text{Ne}^{++}/\text{H}^+)$ and x .

correlation between the degree of discrepancy and the inner extinction found from the Balmer decrement.

(iii) Uncertainties in the atomic data related with the infrared emission of both $[\text{Ne II}]$ and $[\text{Ne III}]$. These emission-lines present some problems as it is evidenced by inspecting the right lower panel of Fig. 1 in which observational data and photoionization models are shown. According to it the models predict systematically lower values of the mid-IR $[\text{Ne III}]/[\text{Ne II}]$ emission-line ratio than observations. This discrepancy was already found by Morisset et al. (2004) and Pérez-Montero & Vílchez (2009) and apparently it is not related with the shape of the used spectral energy distribution in the models. The values for the $[\text{Ne III}]\lambda 15.56\mu\text{m}$ emission-line collision strength found in the literature along decades differ by about 50%. Even when we assume that collision strength for the $[\text{Ne III}]\lambda 15.56\mu\text{m}$ varies by a factor of two, it is not enough to conciliate the neon ionic abundance discrepancy.

(iv) Variations of chemical abundances across the nebula. Using a grid of photoionization models we showed that fluctuations with an amplitude of 0.8 dex in the total abundance (for both O and Ne) can produce the degree of discrepancy between the ionic Ne^{++} abundances derived from optical and mid-IR emission-lines.

Using ionic Ne abundances estimations from mid-IR emission-lines, we obtained an expression for the ICF of the Ne^{++} as a function of the $\text{O}^{++}/(\text{O}^+ + \text{O}^{++})$ ratio. These ICFs obtained through the use of empirical and theoretical derivations of Ne^{++} from mid-IR lines come from a quotient of emissivities and therefore minimize the impact of points

(ii) and (iii) mentioned above, which are more critical for the abundance in absolute value. We then employed a large sample of observational spectroscopic data of star-forming regions compiled from the literature to analyse the dependence of the Ne/O abundance ratio with O/H. We found that Ne/O is about constant with O/H ($\log \text{Ne}/\text{O} \approx -0.70$) for the whole metallicity range considered. This result is independent of the approximation adopted for the ICF, and in all the cases the average Ne/O estimated for our sample is consistent with the adopted solar value.

ACKNOWLEDGMENTS

We are grateful to the referee Dr. Steven Willner for his useful comments and suggestions that helped us to substantially clarify and improve the manuscript. OLD and ACK are grateful to the FAPESP for support under grant 2009/14787-7 and 2010/01490-3. This work has been partially supported by project AYA2010-21887-C04 of the Spanish National Plan for Astronomy and Astrophysics, and by the project TIC114 *Galaxias y Cosmología* of the Junta de Andalucía (Spain). R.Ř. thanks to FAPERGs (ARD 11/1758-5) and CNPq.

REFERENCES

- Allende Prieto, C., Lambert, D. L., Asplund, M. 2001, *ApJ*, 556, 63L
- Amorín, R., Vílchez, J. M., Hägele, G. F., et al. 2012, *ApJL*, 754, L22
- Badnell, N. R., Bautista, M. A., Berrington, K. A. et al. (2006), in *Proc. IAU Symp. 234*, ed. M. J. Barlow, & R. H. Mendez (Cambridge, U.K.: Cambridge Univ. Press), 107
- Baldwin, J. A., Phillips, M. M., & Terlevich, R. 1981, *PASP*, 93, 5
- Bergvall, N., & Östlin, G. 2002, *A&A*, 390, 891
- Blaha, M. 1969, *A&A*, 1, 42
- Bresolin, F. 2011, *ApJ*, 730, 129
- Bresolin, F., Gieren, W., Kudritzki, R. et al. 2009, *ApJ*, 700, 309
- Bresolin, F., Garnett, D. R., Kennicutt, R. C. 2004, *ApJ*, 615, 228
- Bresolin, F., Shaerer, D., González Delgado, R. M., Stasńska, G. 2005, *A&A*, 441, 981
- Butler, K.; Zeppen, C. J. 1994, *A&AS*, 108, 1
- Calzetti, D., Harris, J., Gallagher, J. S., Smith, D. A., Conzelice, C. J., Homeier, N., Kewley, L. 2004, *AJ*, 127, 1405
- Castelli, F., & Kurucz R. L. 2004, *ArXiv Astrophysics e-prints*, ADS, arXiv:astro-ph/0405087
- Copetti, M. V. F., Mallmann, J. A. H., Schmidt, A. A.; Castañeda, H. O. 2000, *A&A*, 357, 621
- Copetti, M. V. F. 2006, *A&A*, 453, 943
- Crockett, N. R., Garnett, D. R., Massey, P., Jacoby, G. 2006, *ApJ*, 637, 741
- Dinerstein, H. L., Lester, D. F., Werner, M. W. 1985, *ApJ*, 291, 561
- Dors, O. L., Jr., Krabbe, A., Hägele, G. F., Pérez-Montero, E. 2011, *MNRAS*, 415, 3616
- Dors, O. L., & Copetti, M. V. F., 2005, *A&A*, 437, 837
- Dors, O. L., & Copetti, M. V. F., 2003, *A&A*, 404, 969

- Drake, J. J., & Testa, P. 2005, *Nat*, 436, 525
- Dufour, R. J., & Harlow, W. V. 1977, *PASP*, 89, 630
- Dufour, R. J., Harlow, W. V. 1977, *ApJ*, 216, 706
- Ellison, S. L., Patton, D. R., Simard, L. et al. 2010, *MNRAS*, 407, 1514
- Engelbracht, C. W., Rieke, G. H., Gordon, K. D. et al. 2008, *ApJ*, 678, 804
- Ercolano, B., Bastian, N., Stasińska, G. 2007, *MNRAS*, 379, 945
- Esteban, C., Bresolin, F., Peimbert, M., Garcia-Rojas, J., Peimbert, A., Mesa-Delgado, A. 2009, *ApJ*, 700, 654
- Firpo, V., Bosch, G., Hägele, G. F., & Morrell, N. 2010, *MNRAS*, 406, 1094
- Firpo, V., Bosch, G., Hägele, G. F., Díaz, A. I., & Morrell, N. 2011, *MNRAS*, 414, 3288
- Ferland, G. J. Korista, K. T., Verner, D. A., Ferguson, J. W., Kingdon, J. B. Verner, E. M. 1998, *PASP*, 110, 761
- Förster, N. M. S., Genzel, R., Lutz, D., Kunze, D., Sternberg, A. 2001, *ApJ*, 552, 544
- French, H. B. 1981, *ApJ*, 246, 434
- García-Rojas, J., Esteban, C., Peimbert, M. et al. 2006, *MNRAS*, 368, 253
- Garnett, D. R., Shields, G. A., Skillman, E. D., Sagan, S. P., Dufour, R. J. 1997, *ApJ*, 489, 63
- Garnett, D. R., Dufour, R. J., Peimbert, M., et al. 1995, *ApJ*, 449, 77
- Garnett, D. R. 1992, *AJ*, 103, 1330
- Garnett, D. R. 1989, *ApJ*, 345, 282
- Garnett, D. R., Edmunds, M. G., Henry, R. B. C., Pagel, B. E. J., Skillman, E. D. 2004, *AJ*, 128, 2772
- Griffin, Mitnik, & Badnell, N. R. 2001, *JPhB*, 34, 4401
- Gordon, K. L., Engelbracht, C. W., Rieke, G. H. et al. 2008, *ApJ*, 682, 336
- Guseva, N. G., Izotov, Y. I., Stasińska, G., Fricke, K. J., Henkel, C., Papaderos, P. 2011, *A&A*, 529, 149
- Guseva, N. G., Izotov, Y. I., Papaderos, P., Fricke, K. J. 2007, *A&A*, 464, 885
- Guseva, N. G., Izotov, Y. I., Thuan, T. X. 2000, *ApJ*, 531, 776
- Grevesse, N., & Sauval, A. J. 1998, *Space Sci. Rev.*, 85, 161
- Hägele, G. F., Pérez-Montero, E., Díaz, A. I., Terlevich, E., Terlevich, R. 2006, *MNRAS*, 372, 293
- Hägele, G. F., Díaz, A. I., Cardaci, M. V., Terlevich, E., & Terlevich, R. 2010, *MNRAS*, 402, 1005
- Hägele, G. F., Díaz, A. I., Terlevich, E., Terlevich, R., Pérez-Montero, E., Cardaci, M. V. 2008, *MNRAS*, 383, 209
- Hägele, G. F., García-Benito, R., Pérez-Montero, E., et al. 2011, *MNRAS*, 414, 272
- Hägele, G. F., Firpo, V., Bosch, G., Díaz, A. I., & Morrell, N. 2012, *MNRAS*, 422, 3475
- Hägele, G. F., Díaz, A. I. Terlevich R., Terlevich, E., Bosch G. L., Cardaci M. V., 2013, *MNRAS*, in press.
- Heydari-Malayeri, M., Charmandaris, V., Deharveng, L. et al. 2002, *A&A*, 381, 941
- Heydari-Malayeri, M., Le Bertre, T., Magain, P. 1988, *A&A*, 195, 230
- Joint SOHO/ACE workshop 201c Solar and Galactic Composition 201d. Edited by Robert F. Wimmer-Schweingruber. Publisher: American Institute of Physics Conference proceedings vol. 598 location: Bern, Switzerland, March 6 - 9, 2001, p.23
- Izotov, Y. I., Papaderos, P., Guseva, N. G., Fricke, K. J., Thuan, T. X. 2006a, *A&A*, 454, 137
- Izotov, Y. I., Stasińska, G., Meynet, G., Guseva, N. G., Thuan, T. X. 2006b, *A&A*, 448, 955
- Izotov, Y. I., Schaerer, D., Blecha, A., Royer, F., Guseva, N. G.; North, P. 2006c, *A&A*, 459, 71
- Izotov, Y. I., & Thuan, T. X. 2004, *ApJ*, 602, 200
- Izotov, Y. I., Chaffee, F. H., Green, R. F. 2001, *ApJ*, 562, 727
- Izotov, Y. I., & Thuan, T. X. 1998, *ApJ*, 500, 188
- Izotov, Y. I., Thuan, T. X., Lipovetsky, V. A. 1997, *ApJS*, 108, 1
- Izotov, Y. I., Thuan, T. X., Lipovetsky, V. A. 1994, 435, 647
- Kaufman & Sugar 1986, *JPCRD*, 15, 321
- Kennicutt, R. C., Bresolin, F., Garnett, D. R. 2003, *ApJ*, 591, 801
- Kessler, M. F., Steinz, J. A., Anderegg, M. E. et al. 1996, *A&A*, 315L, 27
- Kewley, L. J., Rupke, D., Jabran Zahid, H., Geller, M. J., Barton, E. J. 2010, *ApJ*...721L, 48
- Kewley, L. J., Groves, B., Kauffmann, G., Heckman, T. 2006, *MNRAS*, 372, 961
- Kewley, L. J., Jansen, R. A., Geller, M. J. 2005, *PASP*, 117, 227
- Kewley, L. J., Dopita, M. A., Sutherland, R. S., Heisler, C. A., Trevena, J. 2001, *ApJ*, 556, 121
- Kingdon, J. B., & Ferland, G. J. 1995, *ApJ*, 450, 691
- Kingdon, J. B., & Ferland, G. J. 1998, *ApJ*, 506, 323
- Kwitter, K. B., Aller, L. H. 1981, *MNRAS*, 195, 939
- Kobulnicky, H. A., Kennicutt, R. C., Pizagno, J. L. 1999, *ApJ*, 514, 544
- Kobulnicky, H. A., Skillman, E. D., Roy, J.-R., Walsh, J. R., Rosa, M. R. 1997, *ApJ*, 477, 679
- Krabbe, A. C., Pastoriza, M. G., Winge, C., Rodrigues, I., Dors, O. L.; Ferreira, D. L. 2011, *MNRAS*, 416, 38
- Krabbe, A. C., & Copetti, M. V. F. 2006, *A&A*, 450, 159
- Krabbe, A. C., & Copetti, M. V. F. 2005, *A&A*, 443, 981
- Krabbe, A. C., & Copetti, M. V. F. 2002, *A&A*, 387, 295
- Lanz, T., & Hubeny, I. 2003, *ApJS*, 146, 417
- Lebouteiller, V., Bernard-Salas, J., Brandl, B. et al. 2008, *ApJ*, 680, 398
- Lee, J. C., Salzer, J. J., Melbourne, J. 2004, *ApJ*, 616, 752
- Lee, H., Skillman, E. D. 2004, *ApJ*, 614, 698
- Leitherer, C., Schaerer, D., Goldader, J. D. et al. 1999, *ApJS*, 123, 3
- Liu, X.-W., Storey, P. J., Danziger, I. J., Cohen, M., Bryce, M. 2000, *MNRAS*, 312, 585
- López-Sánchez, A. R., & Esteban, C. 2009, *A&A*, 508, 615
- Masegosa, J., Moles, M., Campos-Aguilar, A. 1994, *ApJ*, 420, 576
- Mesa-Delgado, A.; Núñez-Díaz, M., Esteban, C. et al. 2012, *MNRAS*, 426, 614
- McCall, M. L., Rybski, P. M., Shields, G. A. 1985, *ApJS*, 57, 1
- McLaughlin, B. M., & Bell, K. L. 2000, *J. Phys.*, 33, 597
- McLaughlin, B. M., Lee, T.-G., Ludlow, J. A. et al. 2011, *J. Phys.*, 44, 5206
- Mendoza C., 1983, in D. R. Flower ed., *Planetary Nebulae Vol. 103 of IAU Symposium, Recent advances in atomic calculations and experiments of interest in the study of planetary nebulae.* pp1431, 72

- Morisset C., Schaerer D., Bouret J.-C., Martins F. 2004, *A&A*, 415, 577
- Moustakas, J., Kennicutt, R.C. 2006, *ApJ*, 651, 155
- Moustakas, J., Kennicutt, R.C. 2006, *ApJS*, 164, 81
- Nagao, T., Maiolino, R., Marconi, A. 2006, *A&A*, 459, 85
- Nollemberg, J., Skillman, E., Garnett, D. R., Dinerstein, H., 2002, *ApJ*, 581
- Oey, M. S., Meurer, G. R., Yelda, S. et al. 2007, *ApJ*, 661, 801
- Oey, M. S., Dopita, M. A., Shields, J. C., Smith, R. C. 2000, *ApJS*, 128, 511
- Oliveira, V. A., Copetti, M. V. F., Krabbe, A. C. 2008, *A&A*, 492, 463
- Osterbrock, D. E. 1989, *Astrophysics of Gaseous Nebulae and Active Galactic Nuclei* (Sausalito, California, University Science Books)
- Papaderos, P., Guseva, N. G., Izotov, Y. I., Fricke, K. J. 2008, *A&A*, 491, 113
- Pauldrach, A. W. A., Hoffmann, T. L., Lennon, M. 2001, *A&A*, 375, 161
- Peimbert, M., & Costero, R. 1969, *Bol. Obs. Tonantzintla y Tacubaya*, 5, 3
- Peimbert, M., & Torres-Peimbert, S. 1977, *MNRAS*, 179, 217
- Peimbert, M. 1967, *ApJ*, 150, 825
- Peimbert, A. 2003, *ApJ*, 584, 735
- Peimbert, A., & Peimbert, M. 2010, *ApJ*, 724, 791
- Pérez-Montero, E., & Díaz, A. I. 2003, *MNRAS*, 346, 105
- Pérez-Montero, E., Relaño, M., Vílchez, J. M., Monreal-Ibero, A. 2011, *MNRAS*, 412, 675
- Pérez-Montero, E., & Contini, T. 2009, *MNRAS*, 398, 949
- Pérez-Montero, E., Vílchez, J. M. 2009, *MNRAS*, 400, 1721
- Pérez-Montero, E., Hägele, G. F., Contini, T., Díaz, A. I. 2007, *MNRAS*, 381, 125
- Pilyugin, L. S., Vílchez, J. M., Contini, T. 2004, *A&A*, 425, 849
- Pilyugin, L. S. 2001, *A&A*, 369, 594
- Rubin, R. H., Simpson, J. P., Colgan, S. W. J. et al. 2008, *MNRAS*, 387, 45
- Rubin, R. H., Simpson, J. P., Colgan, S. W. J. et al. 2007, *MNRAS*, 377, 1407
- Rubin, R. H., Martin, P. G., Blagrove, K. P. M et al. 2003, *MNRAS*, 340, 362
- Rubin, R. H., Bhatt, N. J., Dufour, R. J. 2002, *MNRAS*, 334, 777
- Rubin, R. H., Dufour, R. J., Geballe, T. R. et al. 2001, in *Astronomical Society of the Pacific Conference Series*, Vol. 247, *Spectroscopic Challenges of Photoionized Plasmas*, ed. G. Ferland & D. W. Savin, 479
- Rubin, R. H. 1989, *ApJS*, 69, 897
- Rubin, R. H. 1985, *ApJS*, 57, 349
- Schaerer, D., & de Koter, A. 1997, *A&A*, 322, 598.
- Simpson, J. P. 1975, *A&A*, 39, 43
- Simpson, J. P., Colgan, S. W. J., Cotera, A. S. et al. 1997, *ApJ*, 487, 689
- Skillman, E. D., Terlevich, R., Melnick, J. 1989, *MNRAS*, 240, 563
- Stanghellini, L., Magrini, L., Villaver, E. Galli, D. 2010, *A&A*, 512, 3
- Stasińska, G. 1978, *A&A*, 66, 257
- Storey, P. J., & Hummer, D. G. 1995, *MNRAS*, 272, 41
- Tang, S., Wang, Q. D., Mac Low, M., Joung, M. R. 2009, *MNRAS* 398, 1468
- Thuan, T. X., & Izotov, Y. I. 2005, *ApJS*, 161, 240
- Thuan, T. X., Izotov, Y. I., Lipovetsky, V. A. 1995, *ApJ*, 445, 108
- Torres-Peimbert, S., Peimbert, M., Fierro, J. 1989, *ApJ*, 345, 186
- van Hoof, P. A. M., Weingartner, J. C., Martin, P. G., Volk, K., & Ferland, G. J. 2001, in *Spectroscopic Challenges of Photoionized Plasmas*, ed. G. Ferland & D. Savin (San Francisco: ASP), ASP Conf Ser., 247, 363
- van Zee, L., Salzer, J. J., Haynes, M. P., O'Donoghue, A. A., Balonek, T. J. 1998, *AJ*, 116, 2805
- van Zee, L. 2000, *ApJ*, 543L, 31
- Vermeij, R., & van der Hulst 2002a, *A&A*, 391, 1081
- Vermeij, R., Damour, F., van der Hulst, J. M., Baluteau, J.-P. 2002, *A&A*, 390, 649
- Vila-Costas, M. B., & Edmunds M. G. 1993, *MNRAS*, 265, 199
- Vílchez, J. M., & Iglesias-Páramo, J. 2003, *ApJS*, 145, 225
- Vílchez, J. M., Pagel, B. E. J., Díaz, A. I., Terlevich, E., Edmunds, M. G. 1988, *MNRAS*, 235, 633
- Vílchez, J. M., Vila-Costas, M. B., & Edmunds, M. G. 1993, *MNRAS*, 265, 199
- Wang, W., & Liu, X.-W. 2008, *MNRAS*, 389L, 33
- Wesson, R., Stock, D. J., Scicluna, P. 2012, *MNRAS*, 422, 3516
- Willner, S. P., & Nelson-Patel, K. 2002, *ApJ*, 568, 679
- Woosley, S. E., & Weaver, T. A. 1995, *ApJS*, 101, 181
- Wu, Y., Bernard-Salas, J., Charmandaris, V., Lebouteiller, V., Hao, L. et al. 2008, *ApJ*, 673, 193